UNIVERSITÀ DEGLI STUDI DI PADOVA

DIPARTIMENTO DI SCIENZE CHIMICHE

CORSO DI LAUREA MAGISTRALE IN CHIMICA

TESI DI LAUREA MAGISTRALE

Colloidal plexcitonic nanosystems based on gold nanorods: design, synthesis and photophysical characterization

Relatore: Prof. ssa Elisabetta Collini

Controrelatore: Prof. Stefano Casalini

LAUREANDA: Caterina Bocchio

ANNO ACCADEMICO 2021/2022

Index

Abstract iii

List of abbreviations v

Introduction 1

Part I: THEORETICAL BACKGROUND 3

1. Description of the light-matter interaction 3

2. Plexcitons: hybrid states originating from the coupling of plasmons and excitons 8

3. Outline of plexcitons dynamics 10

Part II: EXPERIMENTAL METHODOLOGIES 11

4. Nanorods (NR) preparation 11

5. Synthesis of the nanohybrids 12

6. TEM analyses 13

7. Extinction spectra 13

8. Pump-probe technique 13

8.1 Description of the experiment 13

8.2 Optical setup 16

8.3 Fitting models 17

Part III: RESULTS AND DISCUSSION 19

9. Optimization of the synthetic procedures and characterization of gold nanorods 19

9.1 Optimization of the NR synthesis procedure 19

9.2 Optimization of the growth step 21

9.3 Characterization of the oxidized nanorods 24

10. Synthesis and linear optical characterization of the plexcitonic hybrids 30

10.1 Selection of the best molecules for nanohybrids formation 30

10.2 Linear optical characterization 32

10.2.1 Concentration trend 33

10.2.2 Detuning trend 35

11. Non-linear optical characterization 36

11.1 Gold nanorods 37

11.2 PIC J-aggregates 41

11.3 Plexcitons 43

11.3.1 Plexcitons in the 'very strong' coupling regime 44

11.3.2 Strong and intermediate coupled plexcitons 50

11.4 Final remarks on pump-probe measurements 53

Conclusions and future perspectives 57

References 61

Abstract

This Thesis aims at gaining a deeper knowledge of the photophysical properties of hybrid plexcitonic nanosystems. Plexcitons are hybrid states originating from the mixing of the plasmon resonances of metal nanostructures with molecular excitons.

They belong to the family of polaritons, i.e., mixed matter-light states formed upon the promotion of strong coupling between light and matter. These mixed states are currently gaining broad interest to control the flux of energy at the nanoscale thanks to their ability to modify the energy landscape of molecules by promoting strong coupling to an electromagnetic mode.

Here, colloidal plexciton systems are considered, where the plasmonic component is a colloidal nanoparticle. The exploration of the dynamical properties of these nanohybrids is still in its infancy, with just a handful of papers devoted to their ultrafast characterization. Nonetheless, there are high expectations for effectively using the strong coupling to modify rates of chemically relevant molecular processes. The emerging interest in these materials affects several application fields (like sensing, photonics, plasmonic switching and lasing, quantum information processing and artificial light-harvesting) for the chance to obtain useful devices exploiting the peculiar properties of these nanosystems, including their possible capability of sustaining coherent energy transfer.

The research activity has focused first on the synthesis of plexcitonic hybrids, performed by supramolecular coupling of gold nanorods with J-aggregates of the pseudoisocyanine (PIC) molecule. Once fine-tuned and optimized the synthesis procedures, the photophysical properties of the hybrid systems have been characterized and studied with the pump-probe spectroscopy: their ultrafast dynamics are analyzed in different coupling regimes and with different pump fluences. Overall, the obtained findings suggest that in the first few picoseconds,

the hybrid system behaves like the plasmonic moiety. At longer timescales, instead, unique dynamics are found, strongly dependent on the coupling regime.

Preliminary signatures of coherent dynamics between the states have also been found. The obtained results allow drawing essential guidelines to learn how to tune the photophysical and dynamic behavior of these nanomaterials by modifying the experimental parameters involved in their preparation.

The results reported in this Thesis represent an essential step toward developing functional supramolecular materials for quantum-nano-photonic applications.

List of abbreviations

CTAB	Cetyl Trimethyl Ammonium Bromide
ESA	Excited State Absorption
GSB	Ground State Bleaching
L	Longitudinal (plasmon)
LP	Lower Polariton
NR	Nanorods
PIC	Pseudoisocyanine (1,1'diethyl-2,2'-cyanine)
QEs	Quantum Emitters
SE	Stimulated Emission
T	Transverse (plasmon)
TA	Transient Absorption
TEM	Transmission Electronic Microscopy
UP	Upper Polariton

Introduction

This Thesis originates from the interest in studying the coupling between light and matter, which is the subject of intense research activity for the possibility of obtaining devices capable of controlling this particular interaction. The coupling with a light field can significantly modify the properties of the matter system and numerous applications arise in light-emitting devices, sensing, plasmonic switching and lasing, quantum information processing, and artificial light harvesting.[1,2]

In our laboratories, we study new hybrid states known as plexcitons, obtained by the coupling between plasmons and molecular excitations and extremely promising for their dynamic and energy transport properties. However, the photophysics of these states is still in many ways unknown, and their study is one of the scientific hot topics of this decade.

To study plexcitonic nanosystems in a complete way, we initially dealt with the study of the theoretical basis of light-matter coupling and the coupling conditions necessary to obtain hybrids, which will be explained in the first part of this Thesis. Secondly, the analysis continued with the assembly of the nanohybrids. This task required (i) to identify the nanoparticles and the molecular moieties with the most suitable properties to establish a strong coupling regime and (ii) the optimization of all the experimental conditions to achieve this coupling in a controlled and reproducible way.

Therefore, on the one hand, the synthesis procedure of the nanorods (NR) was optimized to obtain nanoparticles with properties suitable for making hybrids. In particular, the reproducibility of the experiments has been tested in order to obtain a valid procedure for further studies. On the other hand, several molecules capable of forming J-aggregates in solution have been considered as the organic

component and Pseudoisocyanine (1,1'diethyl-2,2'-cyanine) PIC has been finally selected.

Once we identified the best plasmonic moiety (oxidized gold nanorods) and excitonic component (J-aggregates of the PIC molecule), we tested the experimental conditions necessary to achieve the plexcitonic nanohybrids. Particular attention has been devoted to verifying how it is possible to control the coupling by acting on experimental conditions such as concentration and detuning between the plasmonic and the excitonic resonances.

Overall, it was possible to fully achieve the control of the synthesis of the nanohybrids and we learned how to tune the system as needed, obtaining precisely the coupling conditions necessary for the specific application required.

Finally, the optical and photophysical properties of the final nanohybrids have been analyzed and characterized in different coupling conditions. In particular, the ultrafast properties were investigated through ultrafast spectroscopy. Systems with different coupling strengths have been considered and a general description of the relaxation dynamics has been reached. Further in-depth studies are required to confirm these preliminary results, but the topic has been revealed to be particularly interesting and full of potential.

Part I: THEORETICAL BACKGROUND

1. Description of the light-matter interaction

The concept of light-matter interaction includes countless cases and, for this reason, it is difficult to find a description at the same time general and exhaustive.

In general, from the classical point of view, we can say that the light-matter interaction occurs when an oscillating electromagnetic field resonantly interacts with charged particles in the matter. Quantum mechanically, light fields will act to couple quantum states of matter.[3] One of the possible ways to control and tune the light-matter interaction is to couple matter systems (molecules, molecular aggregates, inorganic materials) generally defined as Quantum Emitters (QE) with cavities, which are resonant systems[4]. As we will see below, even plasmonic nanoparticles behave like cavities. They are characterized by plasmonic states, which are coherent oscillations of electrons, and for this reason they are also called light-matter dressed states.[1,5–9] In particular, in this Thesis, the attention is focused on nanohybrid systems where the cavity is a plasmonic nanoparticle and the QE is a molecular aggregate characterized by excitonic states.[10–15]

The description of these systems depends on the strength of the interaction between light and matter, i.e., between plasmons and excitons, which can be roughly classified into weak and strong coupling regime.

As it will be discussed later in more detail, this classification is determined by the relative ratio between the value of coupling g between the plasmonic medium and the molecule, the dissipation rate of the molecule γ and the (radiative and non-radiative) dissipation rate of the plasmon κ.[16]

In the case of weak coupling, the plasmon and the exciton maintain their individual properties and the optical response of the excited molecule can be either enhanced or suppressed through the so-called Purcell effect[4,17]. This regime,

widely documented in the literature for plasmonic materials, will not be investigated further in this work.

On the other hand, when g overcomes γ and κ, the system enters the strong coupling regime where g promotes the formation of hybrid states, called plexcitons. [16,18] In this regime, the excited molecule exchanges energy coherently with the plasmonic system faster than any other decay process.[13,17,19,20] It is expected that this coherent coupling alters the properties of both molecules and plasmons. These states have been extensively studied for the propagating surface plasmon polaritons of metal surfaces.[21–25] More recently, strongly coupled plasmon-exciton states have also been identified for the localized surface plasmon resonances of particles.[26]

To describe the formation of these hybrid states and their properties it is necessary to use a quantum mechanical description, referring to the simplest and more general model of a two-level QE that interacts with a single mode of the electromagnetic field[19]. For this system it is possible to write a Hamiltonian that includes contributions from the QE (H_{QE}), the cavity (H_C), and their interaction (H_{int}). It is also convenient to express these contributions in the *rotating wave approximation* and through the Jaynes-Cummings Hamiltonian, from which (Eq 1.1) is retrieved:[3,17,19,27]

$$H = H_C + H_{QE} + H_{int} = \\ = \hbar\omega_C a^+ a^- + \hbar\omega_{QE} |e\rangle\langle e| + \hbar g(|g\rangle\langle e| a^+ + |e\rangle\langle g| a^-) \quad \text{Eq 1.1}$$

with $|g\rangle$ and $|e\rangle$ the ground and excited states of the QE, a^+ and a^- the creation and annihilation operators of the electromagnetic mode and g is the *coupling strength*. When the coupling described by H_{int} is strong enough not to be considered a simple perturbation, then the diagonalization of the Hamiltonian lead to the formation of two new eigenstates, called upper and lower polaritons (UP and LP, respectively) as shown in Figure 1.1a. The resulting eigenfrequencies are:[27]

$$\omega_{\pm} = \frac{\omega_C + \omega_{QE}}{2} \pm \sqrt{\frac{\delta^2}{4} + g^2} \qquad \text{Eq 1.2}$$

where $\delta = \omega_C - \omega_{QE}$ is called the *detuning* between the light and the matter states. Hypothesizing to change ω_C, the detuning δ changes accordingly. The dependence of the UP and LP energies (ħω) on the detuning is shown in Figure 1.1b.[1]

The dashed lines represent the behaviour of the uncoupled light and matter when no coupling occurs. On the contrary, in strong coupling conditions, the trend is completely changed. Far away from the resonance (δ=0), the energies of the uncoupled moieties are practically unchanged. Instead, a so-called avoided crossing behavior is observed near the crossing point (of the non-coupled curves), where there is no detuning.[13,25,28–32] The energy separation between the states at this point is called Rabi splitting, Ω_R.

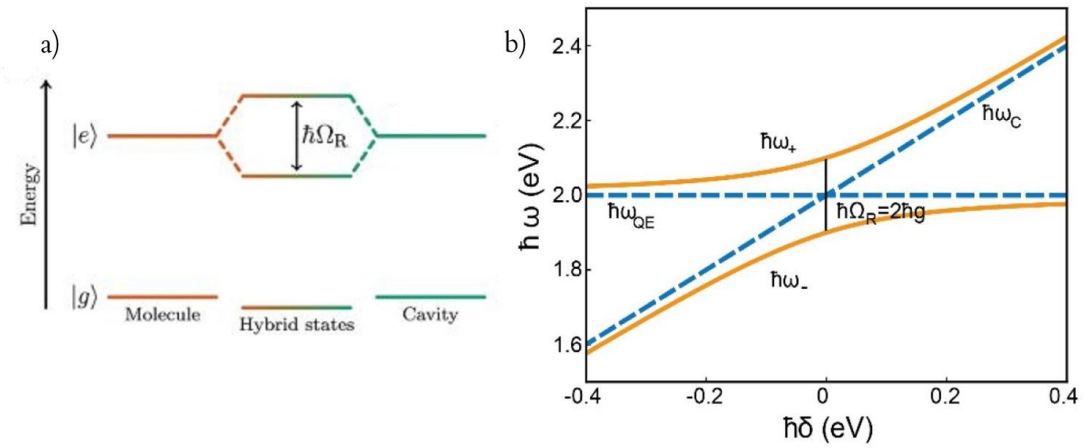

Figure 1.1 a) Schematic representation of the energy levels in the hybrid nanostructure, showing the formation of new hybrid polaritonic states separated by the Rabi splitting $\hbar\Omega_R$. b) Eigenenergies $\hbar\omega_+$ and $\hbar\omega_-$ of the coupled system plotted as a function of the detuning (orange lines). The blue dotted lines represent the energies of the uncoupled cavity and QE.[33] Adapted from references ([19]) and ([9]).

The following eigenstates are found:

$$|+\rangle = \sin(\vartheta_0)\,|g,1\rangle + \cos(\vartheta_0)\,|e,0\rangle \qquad \text{Eq 1.3}$$

$$|-\rangle = \cos(\vartheta_0)\,|g,1\rangle - \sin(\vartheta_0)\,|e,0\rangle \qquad \text{Eq 1.4}$$

where $\sin(\vartheta_0)$ and $\cos(\vartheta_0)$ are defined as follows in Eq 1.5.

$$\sin(\vartheta_0) = \frac{2g}{\sqrt{(R_0-\delta)^2+4g^2}} \qquad \text{Eq 1.5a}$$

$$\cos(\vartheta_0) = \frac{R_0-\delta}{\sqrt{(R_0-\delta)^2+4g^2}} \qquad \text{Eq 1.5b}$$

$$R_0 = \sqrt{\delta^2+4g^2} \qquad \text{Eq 1.5c}$$

The two eigenstates are linear combinations of light and matter states[19]. In resonant conditions and therefore when the transition frequencies of the QE and the cavity match, the polariton can be described as a hybrid state with half matter and half light character[19]. The eigenstates become Eq 1.6 and Eq 1.7:

$$|+\rangle = \frac{1}{\sqrt{2}}(|g,1\rangle + |e,0\rangle) \qquad \text{Eq 1.6}$$

$$|-\rangle = \frac{1}{\sqrt{2}}(|g,1\rangle - |e,0\rangle) \qquad \text{Eq 1.7}$$

These two states are no more independent, and the evolution of the system over time is given by Eq 1.8 from which it is possible to calculate the probability associated with the excitonic and plasmonic states (P_e in Eq 1.9 and P_g in Eq 1.10, respectively):[13]

$$|\Psi(t)\rangle = \cos\left(\frac{\Omega_R t}{2}\right)|g,1\rangle - i\sin\left(\frac{\Omega_R t}{2}\right)|e,0\rangle \qquad \text{Eq 1.8}$$

$$P_e = |\langle e,0|\Psi(t)\rangle|^2 = \frac{1+\cos(\Omega_R t)}{2} \qquad \text{Eq 1.9}$$

$$P_g = |\langle g,1|\Psi(t)\rangle|^2 = \frac{1-\cos(\Omega_R t)}{2} \qquad \text{Eq 1.10}$$

The results are plotted in Figure 1.2 and show that there is a coherent exchange of energy between the cavity and the QE with a frequency that corresponds exactly to the Rabi frequency. [13,17,19,20,33]

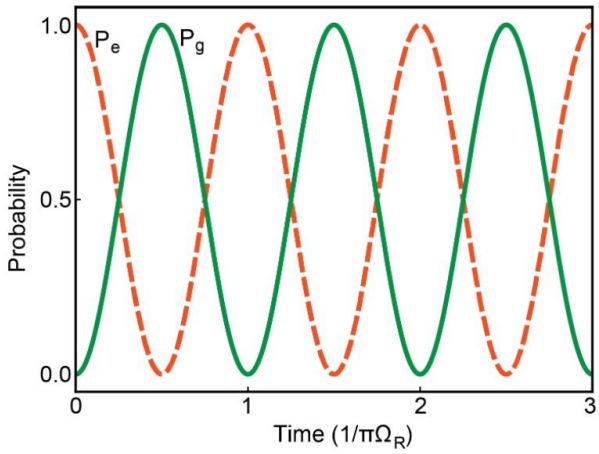

Figure 1.2 Occupancy probabilities P_e and P_g as a function of time. Reprinted from ref. ([33]).

The description until now has neglected the losses of the uncoupled systems but they must be introduced for a meaningful description of the system. To this aim, a complex transition frequency for both the QE and the cavity is defined (Eq. 1.11 and Eq. 1.12):

$$\omega_C' = \omega_C - i\kappa \qquad \text{Eq. 1.11}$$

$$\omega_{QE}' = \omega_{QE} - i\gamma \qquad \text{Eq. 1.12}$$

where γ and κ, as defined before, are the dissipation rates of the molecular exciton and of the plasmon, respectively. [3,16,17] These two quantities can be estimated as the half-width at half maximum (HWHM) of the corresponding bands in the extinction spectra.

The new complex eigenfrequencies and the Rabi splitting become:

$$\omega_{\pm} = \frac{\omega_C + \omega_{QE}}{2} - \frac{i}{2}(\gamma + \kappa) + \frac{1}{2}\sqrt{4g^2 + (\delta - i(\gamma - \kappa)^2)} \qquad \text{Eq. 1.13}$$

$$\Omega_R = \sqrt{4g^2 - (\gamma - \kappa)^2}\,. \qquad \text{Eq. 1.14}$$

To distinguish the strong coupling regime from 'less strong' intermediate regimes, the following conditions can be introduced:

$$2g < |\gamma - \kappa| \qquad \text{Eq. 1.15}$$

$$\Omega_R > \gamma + \kappa \qquad \text{Eq. 1.16}$$

Eq. 1.15 is obtained from Eq. 1.13 in conditions of zero detuning when the term under the square root is positive. This equation illustrates what is defined as the 'condition of existence' of the polaritons. However, this condition alone is not sufficient to ensure that the new polariton states can be resolved one from the other. This is what is described in Eq. 1.16, which requires that the Rabi splitting Ω_R exceeds the polariton full width at half-maximum, i.e., the polaritonic branches can be spectroscopically resolved.[19]

Finally, it can be proved[13,17,19] that the coupling strength is inversely proportional to the square root of the effective volume V of the cavity, and its value is enhanced by a factor $\sqrt{N}$ when considering N QEs coupled to the same cavity (as the excitation is shared among them). These remarks, synthesized in Eq. 1.17, are useful for the following discussion and for the evaluation of the best systems to be chosen for our analyses (see Chapter 2 and Section 10.2.1).

$$g \propto \sqrt{\frac{N}{V}} \qquad \text{Eq. 1.17}$$

2. Plexcitons: hybrid states originating from the coupling of plasmons and excitons

In our analyses, the light-matter interaction is investigated in new hybrid states known as plexcitons, in which the coupling is realized between two quasi-particles that are plasmon and exciton. Plexcitons are a particular example of polarons where indeed the cavity is represented by a plasmonic resonance. Moreover, in our specific case, the excitonic moiety is represented by J-aggregates of dye molecules. These molecules have the property to form highly ordered head-to-tail clusters whose spectroscopic features are completely different from the monomeric form[11].

In particular, their absorption spectrum is dominated by a characteristic very narrow and symmetric absorption peak, red-shifted (towards longer wavelengths) with respect to the monomeric band. Since the linewidth is related to the relaxation rate of the excited state γ [16], these materials are particularly interesting for the achievement of strong coupling systems (see Eq. 1.16 for the strong coupling condition). For this reason, they have been used as QEs for a long time in this research field. On the other side, since plasmons are collective oscillations of free electrons in metals[5], a plasmonic material, like a plasmon nanoparticle and in our case the gold nanorods, plays the role of the cavity. In general nanoparticles have a relaxation decay κ significantly higher than excitons' γ.

Nonetheless, because of their nanometric dimensions, they have the advantage of a very small effective volume V (a few orders of magnitude smaller than the optical cavities), which favors an increased coupling strength (see Eq. 1.17). This feature, in addition to their low cost of production, good stability and scalability, makes them particularly suited in the quest for strongly coupled plexcitonic materials.[34,35] Moreover, for this research project, gold nanorods have been chosen as plasmonic moieties for the particular properties of their plasmon resonances. In fact, as the nanorods have two dimensions (the length and the width), their absorption spectra are characterized by the presence of two plasmonic bands: the so-called 'transverse' peak falls at lower wavelengths (generally around 525 nm) and originates from a mode perpendicular to the long axis, while the 'longitudinal' peak depends on a plasmon oscillation parallel to the long axis and falls at longer wavelengths strictly dependent on the aspect ratio of the two dimensions [5].

The wavelength of the longitudinal peak can be easily tuned by modulating the dimensions and the aspect ratio of the nanorods. This is an additional relevant advantage of these nanoparticles because they allow fulfilling the resonant condition and therefore a possible strong coupling with different J-aggregates.

Lastly, the metal-dye hybrid system is quite easily assembled through supramolecular coupling methodologies. Spontaneous aggregation of the dye molecules is templated on the surface of the plasmon nanoparticles, as previously observed.[36]

3. Outline of plexcitons dynamics

Ultrafast time-resolved techniques, like the pump and probe spectroscopy (see Chapter 8), have only recently started to be applied for the study of the dynamics of these completely new systems. A thorough understanding of the relaxation phenomena is prevented by the complexity of the hybrid electronic states involved. In addition, the lack of a clear and exhaustive definition of the different coupling regimes makes the discussion more challenging and, as a consequence, the interpretation of the dynamic phenomena is much-debated.

What is generally emerging from the first preliminary studies is that typically UP dynamics is expected to be faster than the LP[7,25,37–39] that is considered "intrinsically long-lived"[39,40]. In addition, longer lifetimes for both upper and lower polariton are found for systems where the coupling strength is increased. [25,37]

Several hypotheses have been proposed to justify these phenomena. The most likely is to invoke a significant role of dark states, which might contribute to the relaxation processes from the UP to LP and/or to the redistribution of populations among them. [7,19,39,41] However, the most important evidence emerging from the growing body of time-resolved studies is that the variability of coupled nanosystems and the wide wealth of different measurement conditions make a unified picture extremely complicated. One of the aims of this Thesis is indeed to provide a contribution toward a better understanding of this complicated matter.

Part II: EXPERIMENTAL METHODOLOGIES

All the solvents and reactants were obtained from Sigma-Aldrich (Merck KGaA, Darmstadt, Germany) and used as received without further purification.
Cy78 and TDBC were purchased from Few Chemicals, and PIC was obtained from Sigma-Aldrich (Merck KGaA, Darmstadt, Germany). The dyes were used without further purification.

4. Nanorods (NR) preparation

In a water bath at 27-30 °C, at first 4.92 µL of $HAuCl_4$ (253.9 mM) and 20 µL of MilliQ-water are added to 4.7 mL of CTAB (Cetyl Trimethyl Ammonium Bromide, see Figure 4.1) solution (100 mM) and stirred until the dissolution of the gold. Then, 300 µL of $NaBH_4$ solution (10 mM) are rapidly injected under vigorous stirring: the solution color changes almost immediately from a deep yellow to a light brown color indicating the reduction of metallic gold. The seeds are stored between 27 and 30 °C for two hours and then will be used for the synthesis of single crystal Au nanorods in the ensuing growth step.

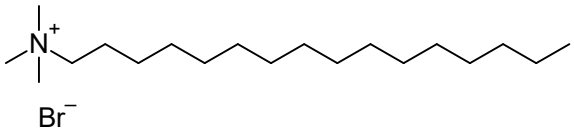

Figure 4.1 Molecular structure of CTAB.

Another solution (the growth solution) is prepared using 10 mL of CTAB solution (100 mM), 190 µL of HCl solution (1M), 19.7 µL of $HAuCl_4$ solution (253.9 mM) and 80 µL of MilliQ water and stirred to dissolve the chloroauric acid. 120 µL of $AgNO_3$ solution (10 mM) are then mixed with this solution, and then 100 µL of ascorbic acid solution (100 mM) are added while gently stirring. The color of the solution changes from pale yellow to colorless. Finally, 24 µL of the seed solution previously made are added, and the growth solution is shaken for 30 minutes and then left undisturbed overnight. The next morning the solutions of as-prepared

nanorods are centrifuged at 8000 rpm for 30 min, redispersed in 1.5 mL of MilliQ water, centrifuged again at 14000 rpm for 6 min and redispersed in 1.5 mL.
For the oxidation step, Au^{3+}-CTAB complex ([Au] = 1mM , [CTAB] = 100 mM) is added dropwise (0.1 mL/min) under magnetic stirring into the vial containing the initial gold nanorods ([Au]=0.5 mM, [CTAB] = 100 mM). The solutions are allowed to react at 30°C for 1 h (under stirring for the first 30 min). Then, the solutions are centrifuged twice (9000 rpm, 40 min) to remove excess gold salt and redispersed in 1.5 mL of milliQ water the first time and in 1 mL of CTAB 15mM the second one.

5. Synthesis of the nanohybrids

Hybrid structures of Au NRs and J-aggregates are produced by adding different amounts of dye solution to 500 µL of an aqueous dispersion of the gold NRs in CTAB, as summarized in Table 5.1. The concentration of the initial solution of nanorods is such that the longitudinal peak has an extinction value of 1. For the concentration trend and the samples "very strong", "strong" and "intermediate" described below (Sections 10.2.1 and 11.3), the amounts of PIC solution in Table 10.1 and 11.2 were added. The solutions are stored overnight, protected from the light, and centrifuged the following day (5 min, 4500 rpm). The precipitates are then redispersed in 0.5 mL of MilliQ water.

Table 5.1. Volumes of dye solution for the preparation of the nanohybrids samples.

Dye	Concentration of the solution	Addition (µL)
PIC	69.07 µM	50
TDBC	1 mM	100
Cy78	1 mM	100

6. TEM analyses

TEM analysis was performed with a Jeol 300 PX electron microscope and the collected images were analyzed with ImageJ software. The results are reported in Figures 9.3, 9.6, 9.7 and Table 9.1.

7. Extinction spectra

Extinction spectra were recorded with a Cary 5000 spectrophotometer.

8. Pump-probe technique

8.1 Description of the experiment

Transient absorption spectra are measured by pump and probe spectroscopy. The technique measures the response of the nanomaterials under the action of two laser pulses, spatially crossed on the sample: the pump, which has the stronger intensity, and the probe, which arrives on the sample at different delay times with respect to the pump. The measured signal is the difference $\Delta I(t)$ between the intensity of the probe beam after application of the pump ($I_P(t)$) and the probe beam alone ($I_{NP}(-\infty)$) as a function of the time delay *t* between the pump and the probe pulses. This differential intensity is then normalized for $I_{NP}(-\infty)$ to obtain the differential transmittance $\Delta T(t)$:[42]

$$\Delta T(t) = \frac{\Delta I(t)}{I_{NP}(-\infty)} = \frac{I_P(t) - I_{NP}(-\infty)}{I_{NP}(-\infty)} \qquad \text{Eq. 8.1}$$

The pump and the probe pulses can be monochromatic pulses at the same wavelength ('one-color' pump-probe) or they can have different wavelengths ('two-colors' pump-probe). Often, as in our case, the probe is a white light continuum containing all the spectral components in the Vis range. In this case, the differential intensity signal can be measured as a function of the time delay *t* and of the probe wavelength λ: $\Delta I(\lambda, t)$. In these conditions, the signal is reported in terms of differential absorption $\Delta A(t, \lambda)$:

$$\Delta A(t,\lambda) = -\log\frac{I_P(t,\lambda)}{I_{NP}(-\infty,\lambda)} = A_P(t,\lambda) - A_{NP}(-\infty,\lambda) \qquad \text{Eq.8.2}$$

Transient absorption (TA) spectra can thus be drawn by plotting the differential absorption $\Delta A(t,\lambda)$ as a function of the probe wavelength λ at a fixed value of the time delay t after pump excitation.

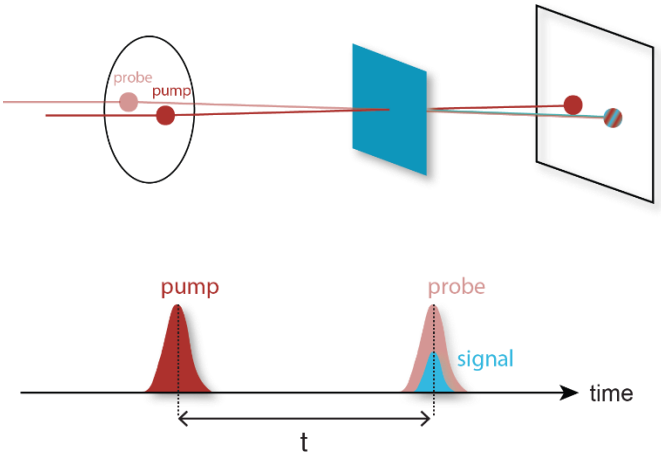

Figure 8.1 Excitation geometry (upper line) and pulse sequence (lower line) for a pump–probe experiment. Adapted from ref ([43]).

In the simple case of a sample with two energy levels, ground (g) and excited (e), and under the hypothesis that the pump and the probe beams are in resonance with the transition $g \rightarrow e$, it is easy to understand that the expected dynamics of the signal as a function of t will follow the behavior schematized in Figure 8.2.

When the pump pulse excites the sample, some molecules are promoted from the ground state to the excited state (red arrow). This means that the concentration of ground-state molecules decreases, and part of the ground state absorption signal disappears. Therefore, at the wavelengths of ground state absorption, the absorption difference becomes negative because the transmitted signal intensity in the presence of the pump (I_P) is higher than the intensity measured without the pump (I_{NP}) (i.e., the transmittance is increased in the presence of the pump). The spectral shape of this negative contribution follows the profile of the ground state absorption spectrum. This contribution to the differential absorption signal is called *ground state bleaching* (GSB). Over time, this signal will decay following the

relaxation dynamics of the excited molecules that return to the original ground state.

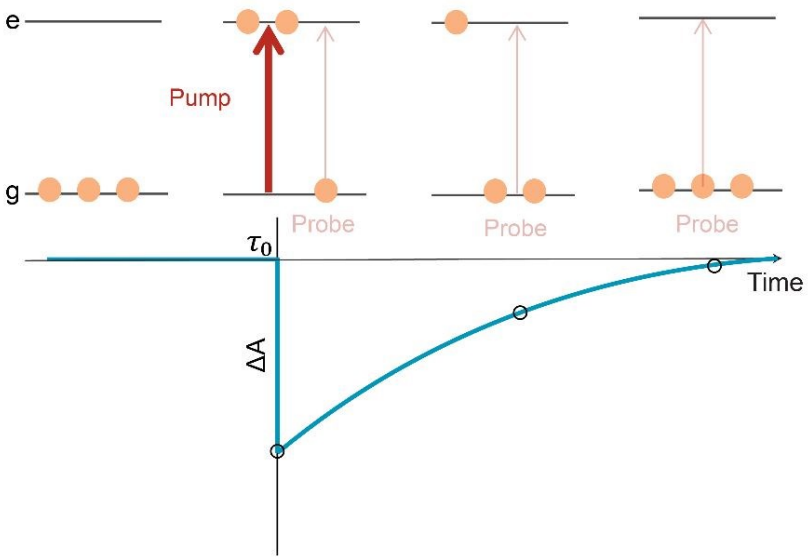

Figure 8.2 Time evolution of a two-level system addressed in a pump and probe experiment (upper line) and the resulting signal output measured as a function of the delay time between pump and probe pulses (lower line). Reprinted from reference (9).

Even if only the GSB is analyzed in the following discussion, two other phenomena are worth to be described: Stimulated Emission (SE) and Excited State Absorption (ESA). The SE arises when the probe pulse finds some of the molecules in the excited state, and the photons of the probe pulse stimulate the emission of the sample molecules (pink arrow in Figure 8.3a). Also in this case a negative signal is recorded because an additional photon is emitted and the transmitted signal in the presence of the pump is higher than the signal without the pump. ESA (Figure 8.3b) is a process that can occur for systems with more than one available excited state when the probe beam causes a further excitation from a first excited state to the next. In this case, the enhanced absorption (i.e., reduced transmittance) leads to a positive signal in the TA spectrum.

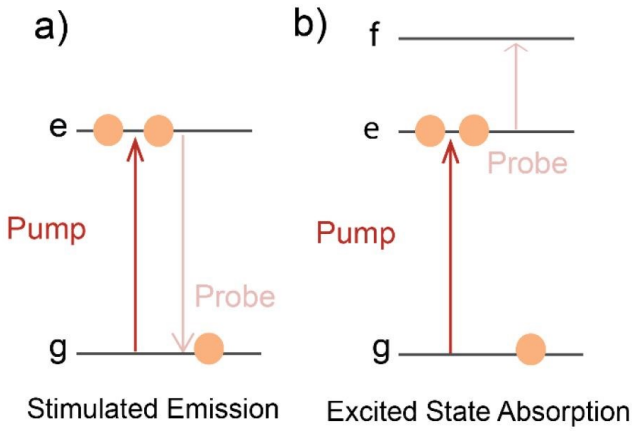

Figure 8.3 Sketch of a) stimulated emission and b) excited state absorption. Reprinted from reference ([9]).

8.2 Optical setup

The home-built pump and probe setup used for the measures reported in this Thesis is described in Figure 8.4.

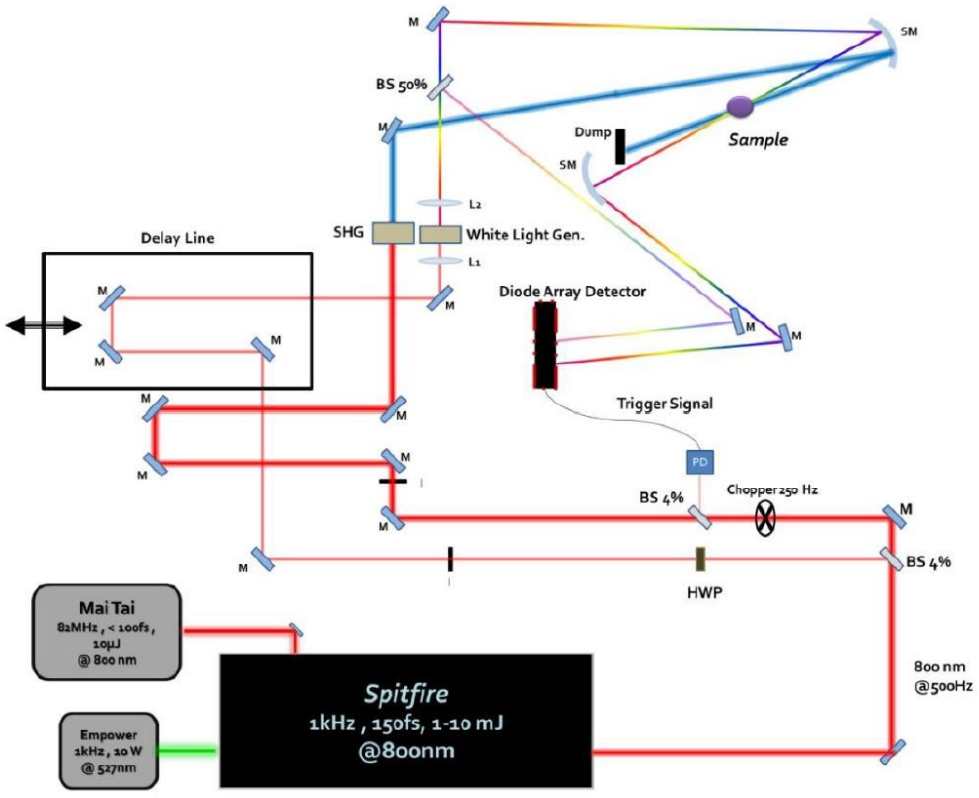

Figure 8.4 Pump and probe setup built in our laboratories. Reprinted from reference ([44]).

The pump and probe beams are generated by an amplified Ti:Sapphire laser (Spitfire, Spectra Physics) seeded by a femtosecond pulsed Ti:Sapphire oscillator (Mai-Tai, Spectra Physics). The laser pulses are emitted at 800 nm, with an energy of 0.8 mJ per pulse, a repetition rate of 1 kHz, and a 160 fs pulse duration. The output laser beam is split by a 4% beam splitter into two paths. The weaker one generates a super-continuum white light in a thin sapphire plate and is used as the probe. The pump pulse at 400 nm is obtained via second harmonic generation in a BBO thin crystal. The pump fluence is tuned from 170 to 900 μJ/cm^2 using neutral OD filters and its repetition rate is halved to 500Hz through an optical chopper. The time delay between the pump and the probe pulses is modulated by a movable delay line inserted in the probe pathway.

The collimated pump pulse and the focused probe pulse are spatially overlapped on the sample. In the overlap region, the pump beam diameter is about 50-70 μm and the probe 20-30 μm. This configuration guarantees that possible small misalignments of the probe beam caused by the motion of the delay line do not cause artifacts in the final TA signal. After the sample, the transmitted probe light is dispersed and directed to a linear CMOS diode array. The quality of the TA signal, i.e., the differential absorption $\Delta A(t, \lambda)$, is improved through repeated measurements and averaging (150-200 measurements were averaged to obtain a sufficient signal-to-noise ratio). The obtained spectra are numerically processed to minimize white light chirping effects, by using a home-made Matlab routine.

8.3 Fitting models

For the fitting of the TA measurements, at least three decay traces in the region of interest are selected and fitted with a global fit with shared time constants. In the analysis, different fitting models have been considered for different samples to account for the diverse nature of the involved states and dynamic processes. The

following equations have been used for the analysis performed on the samples and the results are discussed in Chapter 11.

For the J-aggregates of the PIC molecule, a three exponentials model decay is used:

$$\Delta A(t) = \Delta A_0 + A_1 e^{-\frac{t}{\tau_1}} + A_2 e^{-\frac{t}{\tau_2}} + A_3 e^{-\frac{t}{\tau_3}} \qquad \text{Eq. 8.3}$$

where ΔA_0 is the background value at longer times, τ_i the different time constants and A_i their corresponding pre-exponential factors.

For the uncoupled nanorods samples and plexcitonic nanohybrids, a more complex model has been used to take into account the different nature of the relaxation phenomena, in agreement with the previous literature:[45]

$$\Delta A = \Delta A_0 + A_0 * \left(1 - e^{-\frac{t}{\tau_{i,1}}}\right) * e^{-\frac{t}{\tau_{i,2}}} + A_2 * \left(1 - e^{-\frac{t}{\tau_{i,1}}}\right) * e^{-\frac{t}{\tau_{i,3}}} \qquad \text{Eq. 8.4}$$

Part III: RESULTS AND DISCUSSION

9. Optimization of the synthetic procedures and characterization of gold nanorods

9.1 Optimization of the NR synthesis procedure

Gold nanorods were synthesized with a seed growth protocol[46,47]. The process requires three main steps, nucleation, growth, and oxidation, performed separately (see Chapter 4). Each one of these steps has been deeply analyzed in this research project in order to gain control over the experimental conditions and optimize the synthetic procedure so to obtain time to time NRs with the wanted properties.

The first step – i.e., nucleation - provides the gold seeds, which can be described as very small nuclei made of gold representing the starting point of the nanorods' growth. These small particles are obtained from the solution of $HAuClO_4$ by adding an excess of the strong reducing agent $NaBH_4$ so that all the Au^{3+} is reduced to Au^0. The presence of CTAB in the solution is necessary for the stabilization of the particle and the following growth.

Subsequently, in the growth step, the initially obtained seeds are enlarged, and the growth is performed with a solution containing again chloroauric acid and CTAB. Moreover, the ascorbic acid, acting as a weak reducing agent, is also added so that the chloroauric acid is reduced from Au^{3+} to Au^+. When the seeds are added, the Au^+ of the solutions carries out the growth of the seeds and progressively increases their size, being reduced to metallic gold on the surface of the seeds. Indeed, two possible mechanisms have been proposed: a disproportionation reaction of Au^+ (Eq. 9.1) catalyzed by the seeds, with the subsequent reduction of the new Au^{3+} caused by the remaining ascorbic acid, or a reduction of Au^+ catalyzed by the metallic gold of the seeds which drains electrons from the reductant.[46]

$$Au^{3+} + 2Au^0 \longrightarrow 3Au^{1+} \qquad \text{Eq. 9.1}$$

In addition, a low quantity of HCl is necessary to maintain an acid pH and make the ascorbic acid act as a reducing agent, while small amounts of CTAB and $AgNO_3$ are required to obtain the rod shape. In particular, CTAB provides the rod-like micelle forcing the seeds to an anisotropic growth. Similarly, it is proven that $AgNO_3$ is indispensable for reaching the rod shape, as in its absence no nanorods are formed[46]. In this case, the mechanism is still not clear[8,46]. Although a more detailed description is beyond the scope of this Thesis, some hypotheses have been proposed[8,46–51]. Two of the more accredited are that a silver-bromide interaction could modify the CTAB micelle to favor the rod shape or act as a face-specific capping agent.

As previously explained (Chapter 1), obtaining the strong coupling conditions in the nanohybrids synthesis is the scope of our research. This task requires the fulfillment of the zero-detuning condition, that is the coincidence between the energies of the nanoparticles plasmon and molecular excited states (consequently, the absorption band of the J-aggregates and the longitudinal peak of the nanorods must fall at the same wavelengths). Moreover, we are interested in characterizing the hybrid systems at several detuning conditions, which implies the capability to tune the position of the nanorods' longitudinal plasmon resonance.

The pristine nanorods obtained from the synthesis described above have a longitudinal plasmon peak at approximately 700 nm while the aggregate band position is at 574 nm. Therefore, the next step was to find a procedure to prepare nanorod samples with a blue-shifted longitudinal peak (i.e., falling at shorter wavelengths), corresponding to nanorods with a reduced aspect ratio (see Chapter 2).

For this purpose, the so-called oxidation step is employed, as suggested by the literature[28,38,52]. The reaction requires the addition of small amounts of $HAuClO_4$ to the nanorods solution, in the presence of CTAB. The mechanism is quite simple and employs again the comproportionation between Au^{3+} and Au^0 (Eq. 9.1): the

metallic gold on the nanoparticle surface is oxidized to Au^{1+} because of the presence of Au^{3+} and the nanorods are shortened. The reaction is favored by the presence of CTAB, which changes the equilibrium constants thanks to the binding with $AuCl_4^-$. In addition, the oxidation process is selective for the surface sites with a higher curvature[52] and occurs preferentially at the tips of the nanorods. As a result, the nanorods get reduced only along their longer dimension.

9.2 Optimization of the growth step

By comparing the procedures described in the literature[8,46,48–50,53,54], modifications of the aging time of the solutions before the centrifugation and of the concentrations of Ag^+, ascorbic acid and the amount of seeds are evaluated and finally the protocol previously described is chosen (Chapter 5). In Table 9.1, we report as example how it is possible to modify the longitudinal plasmon wavelength by varying the amount of injected seed solution and the aging time. We found that indeed the aging time is the dominant factor in our protocols.

Table 9.1 Nanorods' samples synthesized with different volumes of seed solution and different aging times: the longitudinal peak is modified according to the different conditions.

Volume of seed solution (μL)	Longitudinal extinction peak wavelength (nm)	
	Aging time: 2 hours	Aging time: overnight
24	NR_4b: 764	NR_4f: 779
50	NR_4c: 760	NR_4g: 776
100	NR_4d: 771	NR_4h: 790

As the extinction spectra are the first way to check the outcome of the synthesis, an initial assessment of the extinction spectra of the non-oxidized samples is made (Figure 9.1a).

First of all, the presence of the two characteristic plasmon bands is an unequivocal sign of nanorods formation: while the transverse plasmon peak has a lower intensity and a quite fixed position at 525 nm, the longitudinal one is more intense

and its position depends on the aspect ratio of the two dimensions of the nanorod (and therefore it is a useful parameter for an estimation of the nanorods' sizes).

It can be noticed that the chosen protocol lets the production of nanorods with a longitudinal peak at approximately 700 nm, with a ratio between the two plasmons' peak intensities of about 3-5, which is comparable with the literature value[46], and no or irrelevant shoulder on the transverse plasmon band. According to the literature, these two parameters are good indicators of the good quality of the synthetized NRs (Figure 9.1b).[46] Another important information that can be extracted from the extinction spectra is the size dispersion. Indeed, when a low size dispersion is obtained, the longitudinal plasmon band is symmetrical and should present a small full width at half maximum (FWHM).

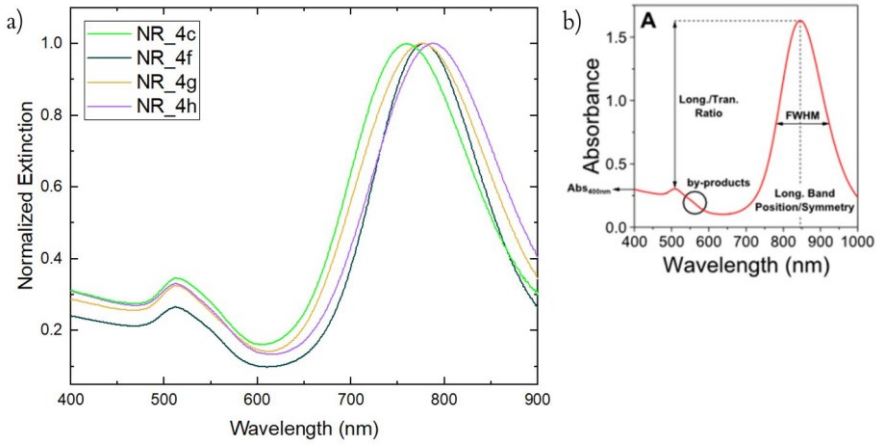

Figure 9.1 a) Comparison between the extinction spectra of selected nanorods prepared using the experimental conditions reported in Table 9.1. b) The definition of the quality parameters as reported in the literature (reproduced from reference ([46])).

The process is quite reproducible. Different solutions of nanorods prepared by starting from the same seed solution through separate growth steps on the same day are characterized by very similar extinction spectra (Figure 9.2a). It is worth pointing out that the reproducibility of the overall synthetic process strongly depends on the initial seed solution. Indeed, nanorods synthesized starting from

seed solutions prepared on different days present slightly different longitudinal plasmon peaks. (Figure 9.2b)

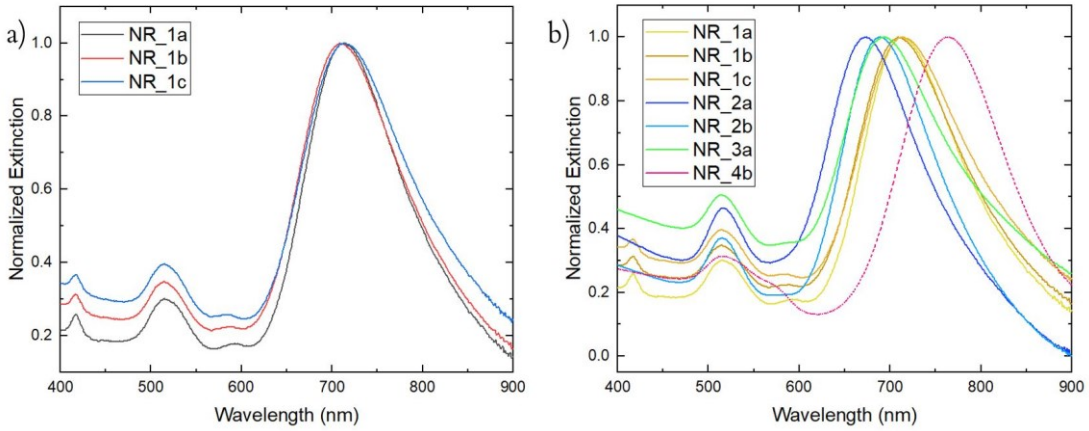

Figure 9.2 a) Extinction spectra of the nanorods NR_1a, NR_1b, NR_1c, synthesized on the same day. b) Extinction spectra of some nanorods prepared on different days and with different seed solutions: the spectra are slightly different.

The TEM analysis confirmed the preliminary findings deduced from the extinction spectra (Figure 9.3).

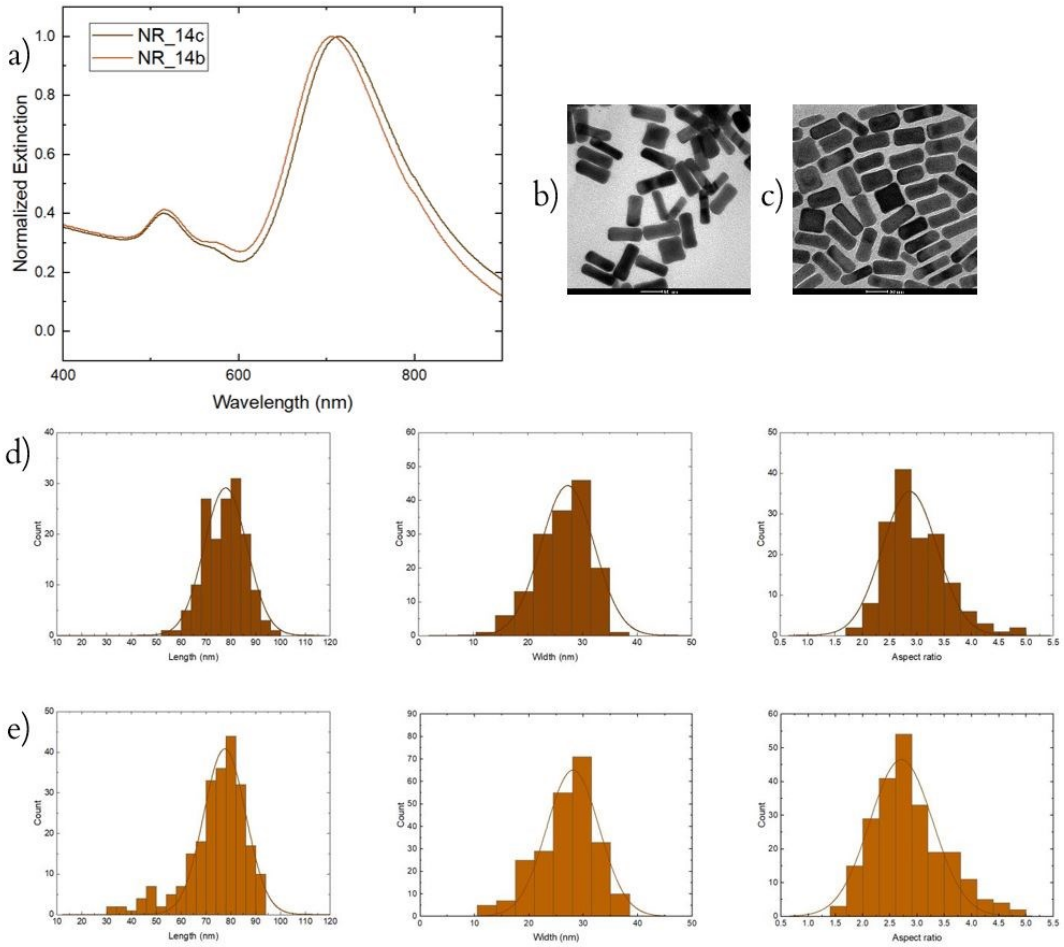

Figure 9.3 a) Extinction spectra of the samples NR_14b and NR_14c, synthesized on the same day. b) and c) TEM images of the nanorods NR_14c and NR_14b, respectively. d) and e) Histograms showing the average dimensions (length, width and aspect ratio) of the samples NR_14c and NR_14b.

9.3 Characterization of the oxidized nanorods

The extinction spectra of some oxidized samples compared with the spectrum of the initial pristine nanorod sample from which they were obtained are shown in Figure 9.4.

The first information one could obtain from the analysis of the spectra is a rough estimate of the concentration of the sample from the value of the extinction at 400 nm. Indeed, it is known that an absorbance of 1.2 at 400 nm corresponds to $[Au^0]$ = 0.5 mM[46].

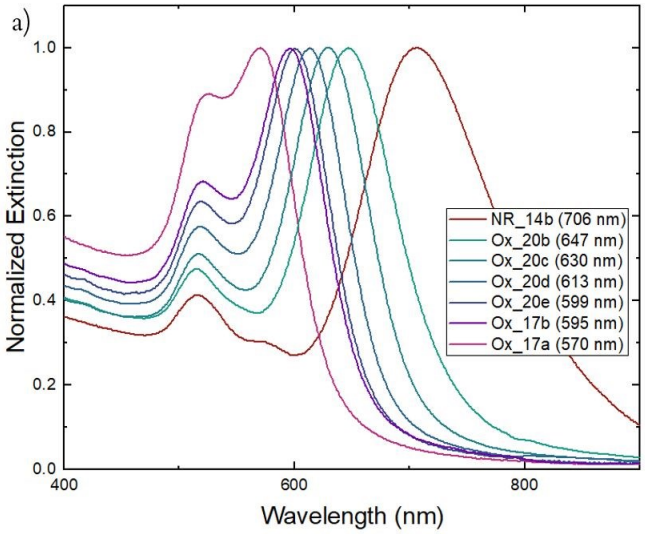

Figure 9.4 a) Extinction spectra of the non-oxidized nanorods (NR_14b) and their oxidized samples.

Table 9.2 Experimental parameters of the oxidation process of the nanorods: [Au^{3+}] concentration used for the procedure, peak wavelengths of transverse and longitudinal plasmons, and average dimensions (length, width and the corresponding aspect ratio) of the samples. The dimensions are calculated by analyzing the TEM images with ImageJ software (Chapter 6).

Sample	Au^{3+} concentration (mM)	Peak wavelength (nm)		Length (nm)	Width (nm)	Aspect Ratio
		Transverse	Longitudinal			
NR_14b	0	515	706	77.6 ± 8.5	28.1 ± 4.8	2.71 ± 0.58
Ox_20b	0.0260	515	647	69.9 ± 8.5	29.8 ± 4.4	2.41 ± 0.36
Ox_20c	0.0477	517	630	66.1 ± 8.4	30.5 ± 4.2	2.201 ± 0.251
Ox_20d	0.0627	518	613	56.1 ± 9.7	30.9 ± 4.1	1.835 ± 0.191
Ox_20e	0.0771	518	599	55.0 ± 11.3	30.0 ± 4.5	1.895 ± 0.241
Ox_17b	0.0969	520	595	57.1 ± 8.8	30.4 ± 4.5	1.858 ± 0.183
Ox_17a	0.1245	525	570	49.7 ± 8.7	30.8 ± 3.5	1.619 ± 0.182

As expected, we found that the blue shift of the longitudinal plasmon peak of the oxidized samples could be enhanced by increasing the amount of Au^{3+} added. The obtained trend is summarized in Table 9.2.

Analogously, the TEM analyses show that proceeding with the oxidation (i.e., increasing the concentration of Au^{3+} in the reaction mixture), the oxidized samples progressively reduced their length, while the width remains substantially unchanged (see Figure 9.5a). The same trend is recognizable looking at the longitudinal peak energy shown in Figure 9.5b.

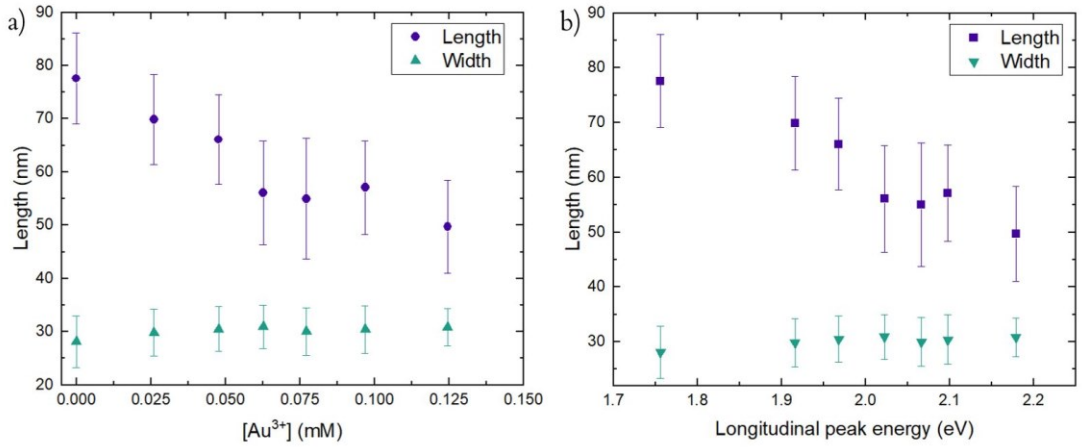

Figure 9.5 Comparison between the dimensions of the oxidized samples (length and width) as a function of the concentration of Au^{3+}(a) and the energy of the longitudinal peak (b).

The most oxidized sample can still be considered a nanorods sample because it has the same shape as the initial nanoparticles except for more rounded tips (see Figure 9.6). Indeed, it may be noticed that the oxidation actually proceeds from the tips, especially starting from the angles, confirming the suggested hypothesis of selectivity dependence on higher curvature sites.

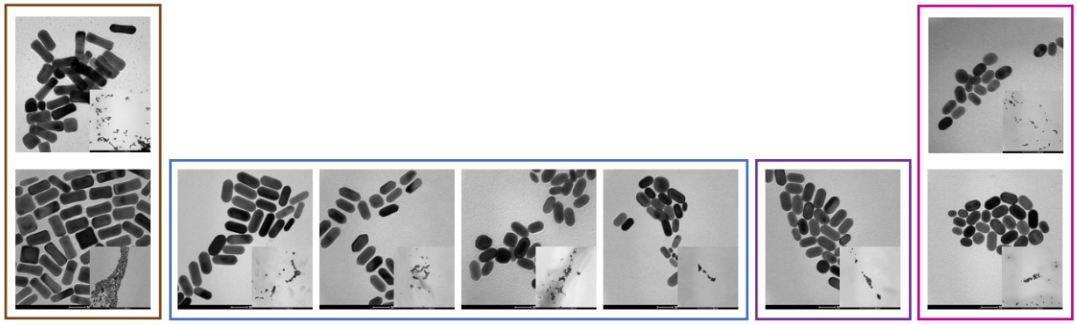

Figure 9.6 TEM images of the nanorods: non oxidized nanorods (samples NR_14c and NR_14b) in the brown frame; oxidized Ox_20b, Ox_20c, Ox_20d, Ox_20e, Ox_17b samples in the blue and violet frame; in the purple frame the most oxidized samples Ox_17a and Ox_16a.

As for the initial nanorods, oxidized samples prepared from different batches of synthesis have similar dimensions if their extinction spectra show longitudinal peaks at approximately the same position (Figure 9.7a).

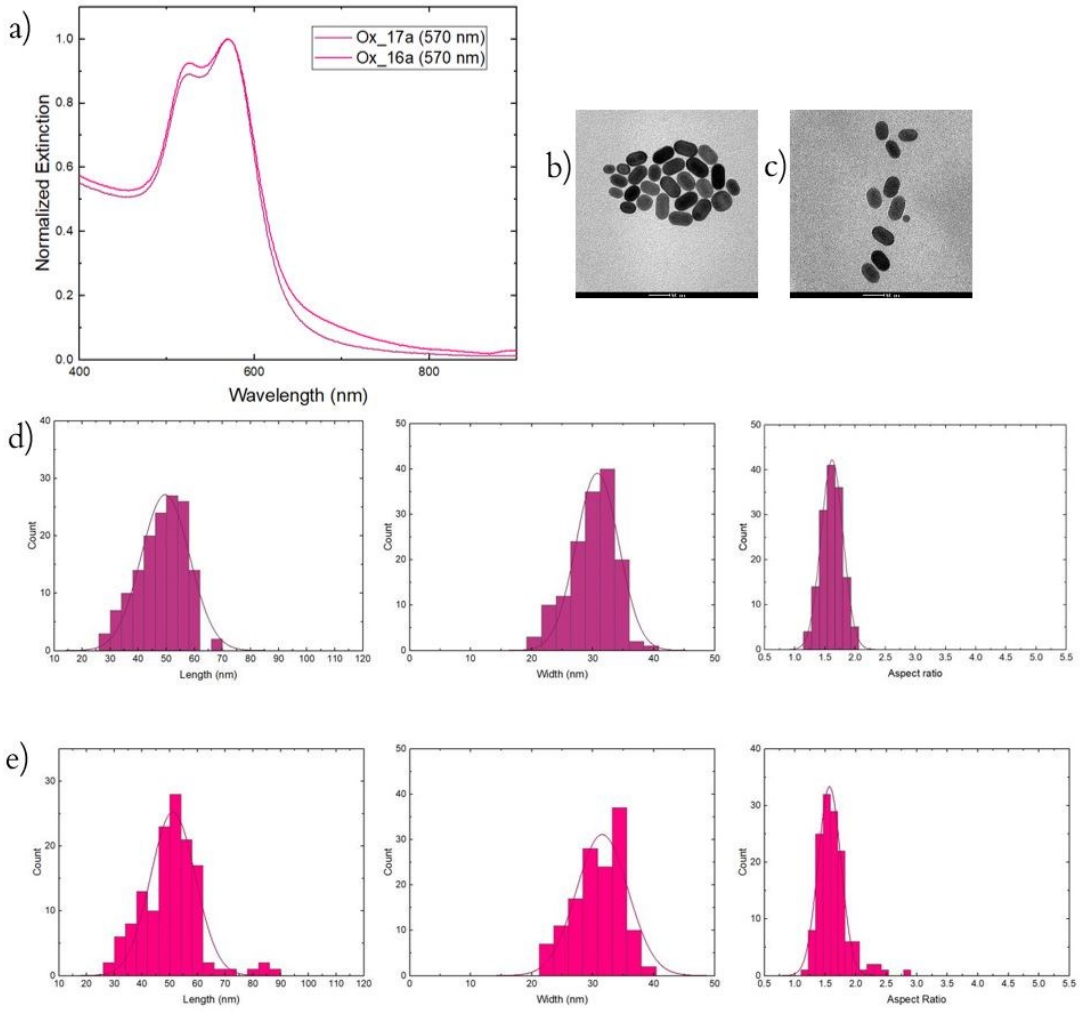

Figure 9.7 a) Extinction spectra of the samples Ox_17a and Ox_16a and their TEM images, b) and c), respectively. d) and e) Histograms showing the average dimensions (length, width and aspect ratio) of the samples.

From these observations and based on the data reported in Table 9.1, it should be possible to predict the oxidation trend and set the experimental conditions so to obtain the nanorods with a longitudinal plasmon peak at the exactly wanted wavelength. However, we found that this is not fully possible. Indeed, although a predictable behavior is always found for nanorods synthesized on the same day (we found a linear dependence of the plasmon resonance wavelength as a function of the oxidizing species Au^{3+}, Figure 9.8), no common trend was found for nanorods prepared in different days, suggesting a non-fully controllable dependence on the initial conditions of synthesis. To explain this behavior, it is hypothesized that the

most relevant aspect may be the presence of traces of by-products. Their unpredictable shape and quantity affect the oxidation yield of the nanorods in such a way that it is impossible to make any prediction. To overcome this issue, for each batch of synthesis we first performed an oxidation test, to identify the specific trend ΔE vs [Au^{3+}] for that specific sample. Then, this information was used to calibrate the experimental conditions in order to obtain nanorods with the wanted properties.

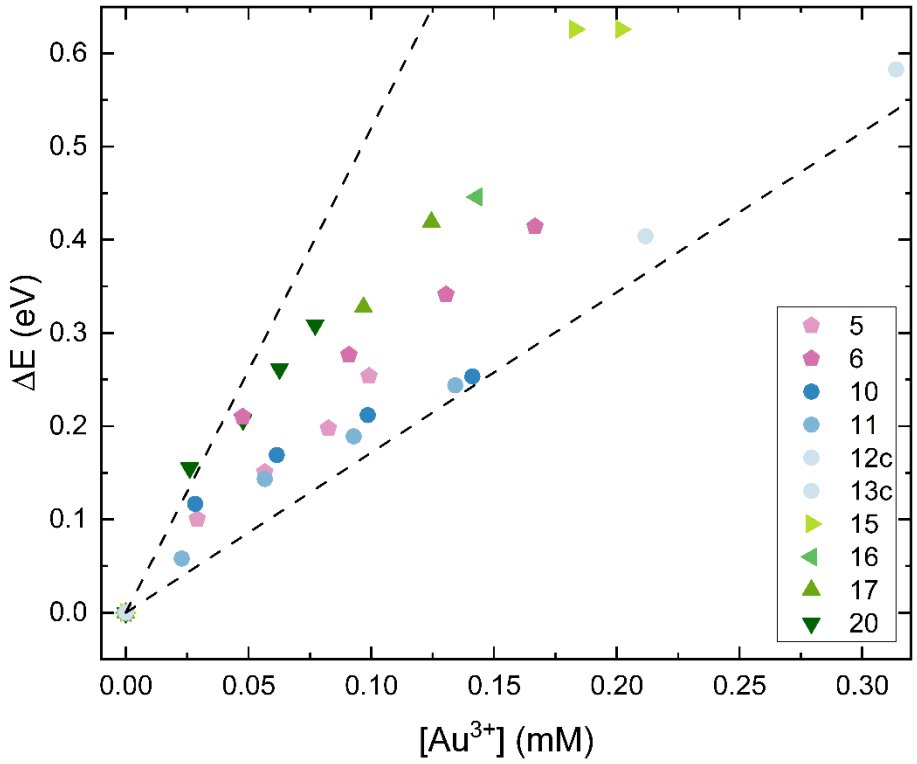

Figure 9.8 Energy difference between the longitudinal peak in the non-oxidized nanorods and the longitudinal peak obtained after the oxidation (ΔE) plotted as a function of the concentration of Au^{3+} employed in the oxidation step. Different colors (pink, blue, green) refer to nanorods synthetized starting from different seed solutions.

10. Synthesis and linear optical characterization of the plexcitonic hybrids

10.1 Selection of the best molecules for nanohybrids formation

As explained in Chapter 2, the hybrid nanosystems were assembled by promoting supramolecular interactions between the nanorods and the organic molecules.

At first, three different cyanines (1,1-diethyl-2,2-cyanine (PIC), Cy78 and TDBC) were selected for the realization of the nanohybrids. Their molecular structure is reported in Figure 10.1. All the three molecules are known to form J-aggregates, and therefore, in principle, they should all be able to strongly couple with nanorods since the γ factor is expected to be favorable in all cases (see Equation 1.15 and Chapter 2). Nonetheless, the three molecules have different charges and shapes, and this can lead to different results in terms of supramolecular coupling.

Looking at the molecular structure of the three molecules, shown in Figure 10.1, it is immediately evident that the PIC molecule has a positive charge and smaller dimensions; on the contrary, the TDBC and Cy78 molecules are anionic and occupy a bigger volume because of the bigger dimensions.

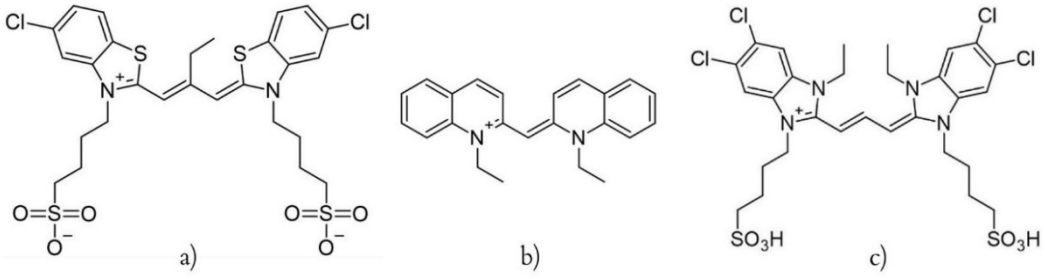

Figure 10.1 Molecular structure of a) Cy78, b) PIC, c) TDBC.

To check the capability of the three molecules to interact with the nanorods and form plexcitonic nanohybrids, a suitable amount of the cyanine solutions was added to solutions of nanorods. In order to achieve a meaningful comparison

between the performances of the three molecules, attention was paid to using the same conditions and adding the same amounts of molecules (see Chapter 5 and Table 5.1).

To achieve the strongest possible coupling, the plasmonic and excitonic systems must fulfill the resonance conditions. Therefore, slightly different nanorod samples were used in combination with the three different cyanine molecules, so to have a longitudinal plasmon falling at the same wavelength as the absorption band of each cyanine J-aggregate (574 nm for the PIC, 590 for the TDBC and 620 for the Cy78).

The formation of strongly coupled plexcitonic nanohybrids was then tested by recording the extinction spectra. Indeed, the formation of two new hybrid plexcitonic states (LP and UP) is manifested in the extinction spectra by the appearance of a dip in the broad plasmon resonance. This dip is the clear manifestation of an avoided crossing point (see Chapter 1, Figure 1.1), whose position in wavelength corresponds exactly with the J-aggregate excitonic resonance. The distance in energy between the two newly formed peaks can be used to estimate the Rabi splitting and the coupling (see Chapter 1). [1,19,30]

While no coupling is obtained with the TDBC J-aggregate, interesting results are achieved for the PIC and the Cy78 J-aggregates. In Figure 10.2, the extinction spectra of the hybrids are shown and compared with the spectra of the two non-coupled constituents measured separately.

The J-aggregate peaks of the two cyanines are at 574 and 618 nm, both almost in resonance with the two nanorods' longitudinal peaks at 591 and 621 nm, respectively. In both spectra, the typical splitting of the longitudinal band of the gold nanoparticles is recognizable. These two split bands are associated with the formation of hybrid plexcitonic states[1,19,30] and, as anticipated before, the splitting and the energy distance between these two bands reflect the strength of the

coupling. Thus, by comparing the spectra of the nanohybrids formed with PIC and Cy78, it can be noticed that in the first case a much stronger coupling could be obtained. This led to the choice of PIC for all the ensuing analyses and characterizations.

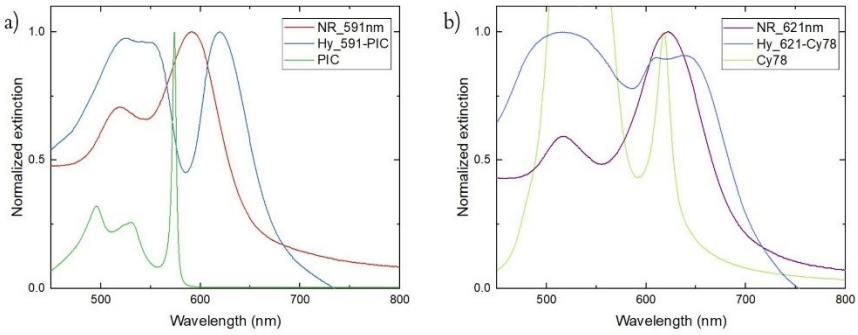

Figure 10.2 Extinction spectra of the nanohybrids (blue lines) compared with their pristine nanorods (red and purple lines) and dye molecules (green curves). (a) Hy_591-PIC and (b) Hy_621-Cy78, obtained using PIC and Cy78 molecules, respectively.

10.2 Linear optical characterization

As previously explained in Chapter 1, the strong coupling regime can be defined based on the Rabi splitting measured from the extinction spectra, which provide the first experimental proof of the formation of two hybrid plexcitonic states [1]. Following the typical procedure documented in the literature[14,28–31,55], to characterize the effective formation of plexcitonic hybrids, it is first necessary to perform an analysis of the trend of the Rabi splitting as a function of the added volume of molecules' solution. This procedure leads to the evaluation of the coupling strength related to the number of molecules (often referred to as 'the concentration trend').

Secondly, it is common to analyze also the 'detuning trend', which allows studying the trend of the Rabi splitting when the plasmon and exciton energies are out of resonance, and how the coupling conditions are modified by increasing the detuning between the plasmon and exciton states.

10.2.1 Concentration trend

In order to verify the 'concentration trend', several plexcitonic systems are prepared using different amounts of PIC molecules by adding different volumes of a PIC solution 69 μM, as shown in Table 10.1. The extinction spectra of the resulting samples, before and after the centrifugation, are recorded and some of them are shown in Figure 10.3, where they are also compared with the spectra of nanorods and dye measured separately. In addition, in Figure 10.4 the added volume versus the calculated Ω_R is plotted. In agreement with the literature, increasing the added volume of the dye molecules increases the coupling, until the strongest coupling conditions are reached.[14,55] Furthermore, according to Equations 1.16 and 1.15, reported in Chapter 2, the limit of strong coupling ($\Omega_R > \gamma + \kappa$) and the limit of weak coupling ($2g < |\gamma - \kappa|$) are also indicated with pink and orange lines, respectively. From these results it is clear that the system can be tuned to obtain the required coupling condition by simply modifying the amount of PIC solution added.

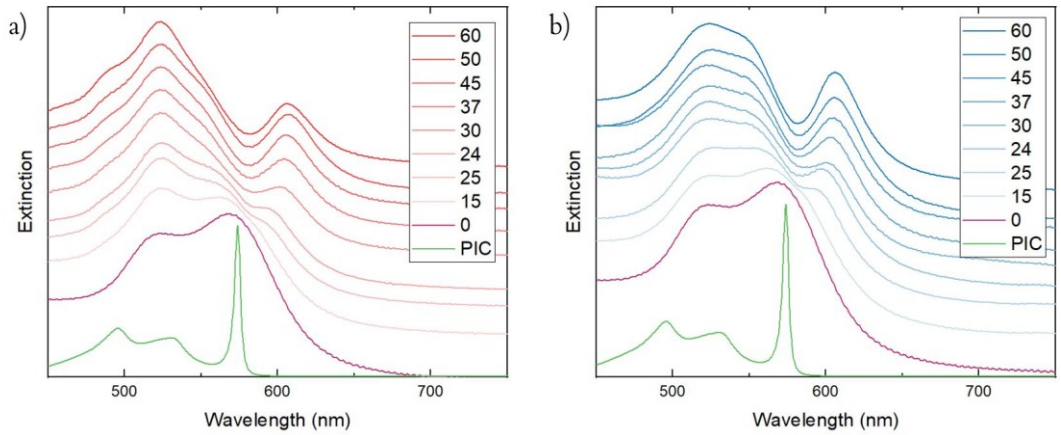

Figure 10.3 Extinction spectra of the nanohybrids synthesized with the experimental conditions reported in Table 10.1, before (a, red curves) and after (b, blue curves) centrifugation. In green the extinction spectra of the dye (PIC), in purple the bare nanorods.

Table 10.1 Study of the concentration trend: volume of PIC solution added for the nanohybrids synthesis and corresponding Rabi splitting as estimated from the extinction spectra.

Sample	Volume (μL) of PIC solution (69 μM) added	Rabi splitting Ω_R (meV)
Ox_17a	0	0
Hy_18a	2	0
Hy_18b	5	0
Hy_18c	10	0
Hy_18d	15	56
Hy_18f	25	135
Hy_18e	24	169
Hy_19a	30	203
Hy_19b	37	217
Hy_19c	45	225
Hy_18g	50	241
Hy_19d	60	241
Hy_19e	75	237

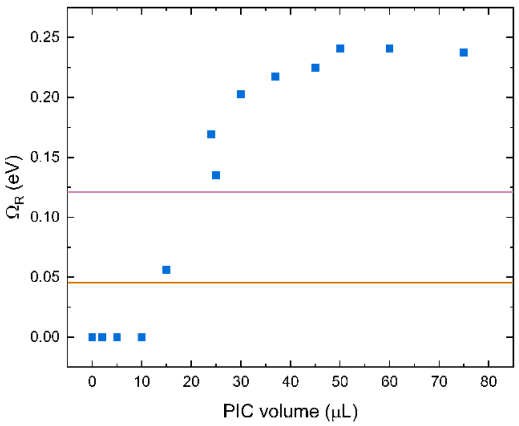

Figure 10.4 The Rabi splitting Ω_R is plotted as a function of the added volume of dye molecules. The pink line represents the strong coupling limit condition (Eq. 1.16), the orange line the existence condition limit (Eq. 1.15).

10.2.2 Detuning trend

For the detuning trend, several hybrid samples are prepared, using the same volume of PIC solution (50 μL) added to different nanorod samples, as reported in Table 10.2.

In Figure 10.5, the energy values of the upper and lower plexciton resonances are plotted as a function of the longitudinal plasmon peak. The resulting trend shows the characteristic plexcitonic anti-crossing behavior.[13,14,28–31,55] At zero detuning the energy splitting assumes the minimum value, the two components are in resonance conditions and the crossing point is missing. As the detuning gets increased, the two peaks become more similar to the original signals of the non interacting nanorods and J-aggregates.[13,14,28–31,55]

Table 10.2 Spectroscopic parameters emerging from the study of the detuning trend. The position of the plexcitonic resonances is compared with the position of the longitudinal peak of the bare nanorods for selected samples.

Sample	Longitudinal wavelength of the bare nanorods (nm)	Upper plexcitonic resonance (nm)	Lower plexcitonic resonance (nm)
21a	704	709	575
21b	647	656	568
21c	630	642	565
21d	613	617	573
21e	600	621	556
21f	591	616	553

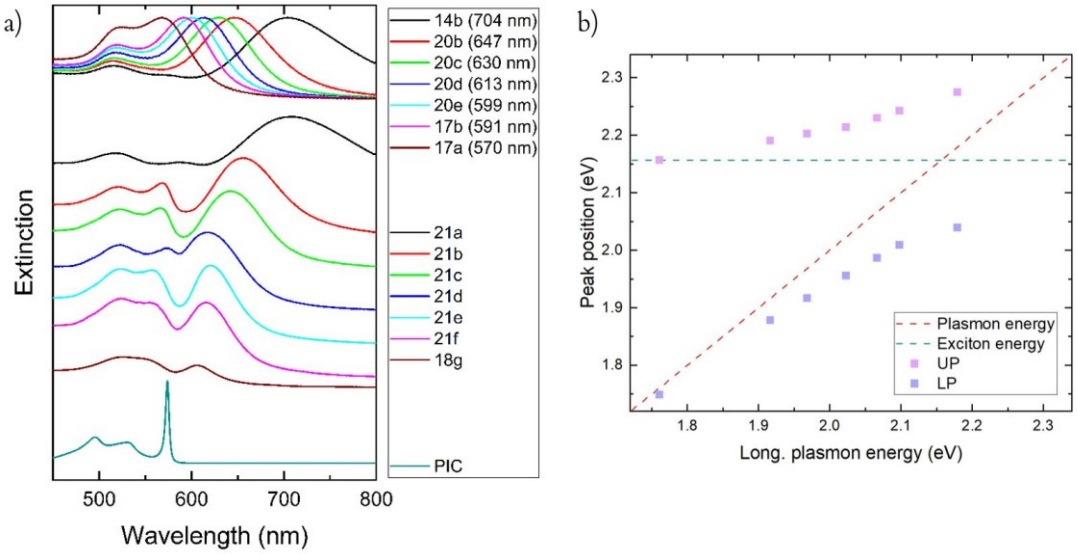

Figure 10.5 a) Extinction spectra of the samples described in Table 10.2: in the top, the bare nanorods, in the middle the nanohybrids, in the bottom the dye molecule. b) The anticrossing beaviour of plexcitons (see Chapter 1): far away from the resonance, the energies of the uncoupled moieties are practically unchanged and are overlapped with the dashed lines describing the behavior of the pristine nanorods and J-aggregates. Instead, an avoided crossing behavior is observed near the crossing point (of the non-coupled curves), where there is no detuning (δ=0).

11. Non-linear optical characterization

One of the aims of this Thesis was to characterize the dynamic properties of plexciton nanohybrids in the femtosecond time domain, comparing the behaviour of samples in different coupling conditions. This was achieved by measuring TA spectra by pump and probe spectroscopy. However, to be able to provide a correct interpretation of the dynamic behavior of the nanohybrids and clearly identify the unique features emerging only upon the establishment of strong coupling between the NR and the molecular dyes, the preliminary study of the dynamic behaviour of the uncoupled species (NRs and molecular J-aggregates) in the same experimental conditions is necessary. These data are taken as a reference for the investigations on plexciton systems.

11.1 Gold nanorods

Transient absorption spectra of a selected sample of oxidized nanorods (sample Ox_25b, with extinction spectrum shown in Figure 11.1) are collected using three different values of pump fluences.

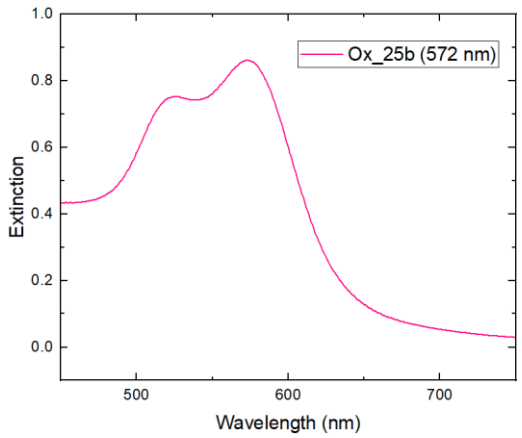

Figure 11.1 Extinction spectrum of the oxidized nanorods Ox_25b with longitudinal peak at 572 nm.

The transient spectra at selected values of delay times are shown in Figure 11.2a. The spectra are dominated by two strong ground state bleaching (GSB) signals at 527 and 574 nm, assigned to the two plasmon bands.

The dynamics of the GSB recovery are followed at the wavelengths corresponding to the two plasmon peaks and shown in Figures 11.2d and 11.2e, for the longitudinal and transverse resonances, respectively. In agreement with the literature, we found three decay times for both the transverse and longitudinal peaks dynamics:

i) an early rise of the transient bleach with a time constant $\tau_{nr,1}$ (0.260±10% and 0.190±10% ps for the transverse and the longitudinal peak, respectively) is found to occur in a timescale comparable with the excitation pulse duration and assigned to electron-electron scattering[8,56];

ii) a fast decay of a few picoseconds $\tau_{nr,2}$ (2.66–7.69 ps for the transverse and 2.12–5.78 ps for the longitudinal peak) is attributed to electron-phonon relaxation processes[57–59];

iii) a slow decay dominates the late time dynamics with a time constant of hundreds of picoseconds $\tau_{nr,3}$ (286±10% and 329±10% ps), which is ascribed to the phonon-phonon relaxation from the particle to the surrounding solvent[57–59].

The kinetic constants found in three different conditions of pump fluence are reported in Table 11.1 and the plots summarizing all the data can be found in Figure 11.3.

Table 11.1 Kinetic constants of the nanorod sample Ox_25b for the transverse and longitudinal peaks in different conditions of pump fluence.

Pump fluence ($\mu J/cm^2$)	$\tau_{nr,1}$ (ps)	
	Transverse peak decay time	Longitudinal peak decay time
170	0.426 ± 0.013	0.237 ± 0.009
394	0.284 ± 0.008	0.198 ± 0.006
888	0.188 ± 0.007	0.166 ± 0.005
$\tau_{nr,2}$ (ps)		
	Transverse peak decay time	Longitudinal peak decay time
170	2.74 ± 0.04	2.14 ± 0.03
394	3.72 ± 0.04	2.83 ± 0.03
888	7.69 ± 0.12	5.78 ± 0.06
$\tau_{nr,3}$ (ps)		
	Transverse peak decay time	Longitudinal peak decay time
170	354 ± 34	415 ± 57
394	320 ± 22	519 ± 46
888	335 ± 17	582 ± 43

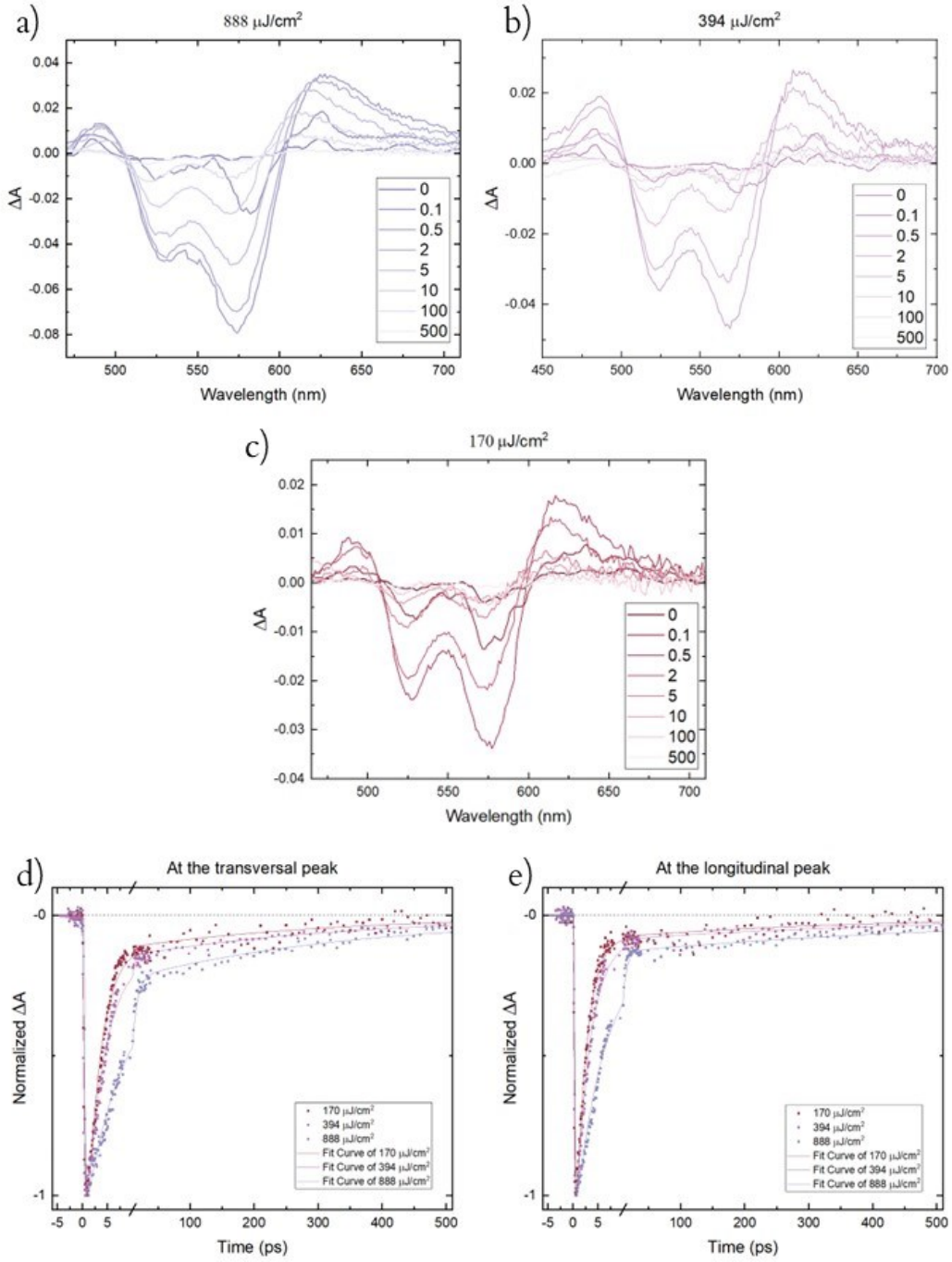

Figure 11.2 Transient absorption spectra recorded at different delay times (in the legend the delay in ps), using three different pump fluences: 888 μJ/cm² (a), 394 μJ/cm² (b) and 170 μJ/cm² (c). In (d) and (e), the decay curve extracted at wavelengths corresponding to the transversal and longitudinal peaks. Notice the break in the time axis after 10 ps.

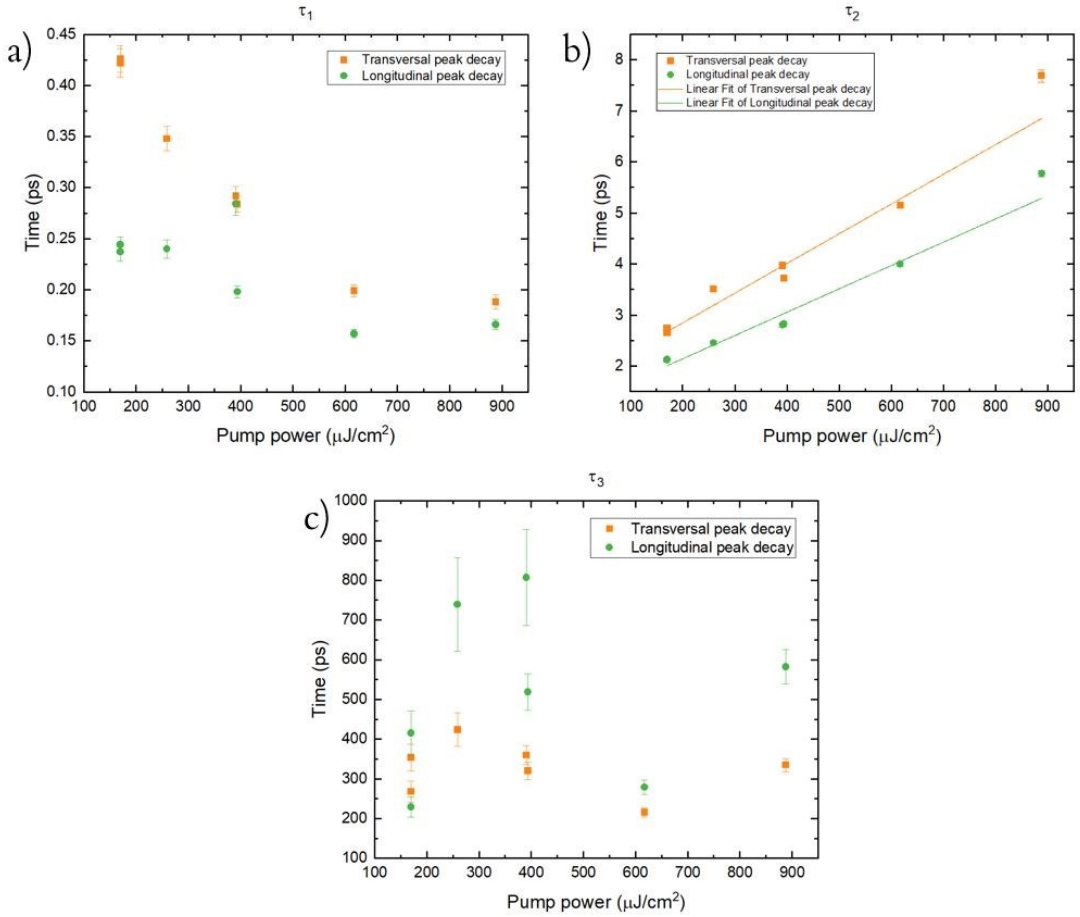

Figure 11.3 Dependence of the kinetic constants of NRs on the pump fluence (see Table 11.1): (a) $\tau_{nr,1}$ *. (b)* $\tau_{nr,2}$ *. The solid lines (orange and green) represent the fit with equation:* $y = 0.0058 * x + 1.70$ *and* $y = 0.0046 * x + 1.24$ *for the transversal and longitudinal time constants, respectively. (c)* $\tau_{nr,3}$ *.*

It is important to note that the time constant associated with the electron-phonon processes shows a clear dependence on the pump fluence: indeed, $\tau_{nr,2}$ increases as the pump fluence is increased. This finding is a direct consequence of the higher initial temperature of the electron gas reached at higher fluence values, which is then dissipated more slowly to the lattice.[60] According to the literature,[60] also the electron-electron scattering dynamics should be fluence dependent. This dependence, however, is not fully noticeable in our data because the timescale of the process is very close to the experimental time resolution (pulse duration) leading to a higher uncertainty in the time constants determination.

11.2 PIC J-aggregates

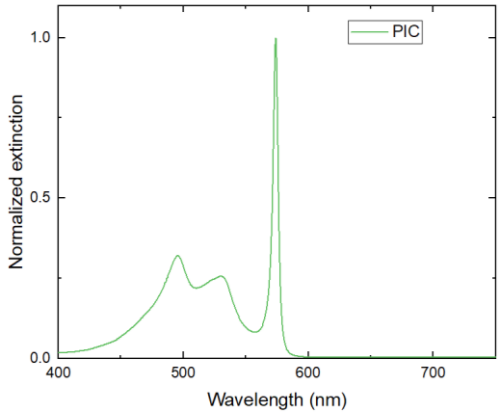

Figure 11.4 Extinction spectrum of the PIC J-aggregates.

The transient absorption spectra of the PIC J-aggregates (the associated linear extinction spectrum is reported in Figure 11.4) are characterized by a strong GSB signal at 583 nm and a blue-shifted excited state absorption (ESA) at 578 nm, as shown in Figure 11.5a,b,c. The dynamics of the GSB signal can be fitted using a three-exponential decay model:

i) a fast component $\tau_{PIC,1}$ of duration shorter than the pump pulse duration (< 150 fs). Even if the time constant is not quantifiable in our experimental conditions, the associated process can be identified and ascribed to the ultrafast relaxation of two-exciton states following the photoexcitation at 400 nm[61,62];

ii) a time constant of a few picoseconds $\tau_{PIC,2}$ (between 1.2 and 3.9 ps) is attributed to the exciton-exciton annihilation process and, as expected for this kind of phenomena, is dependent on the pump fluence[61,62];

iii) an additional fluence dependent lifetime $\tau_{PIC,3}$ between 24 and 39 ps, is detected and can be ascribed to the fluorescence lifetime of the PIC J-aggregate, as already found in the literature[63–66].

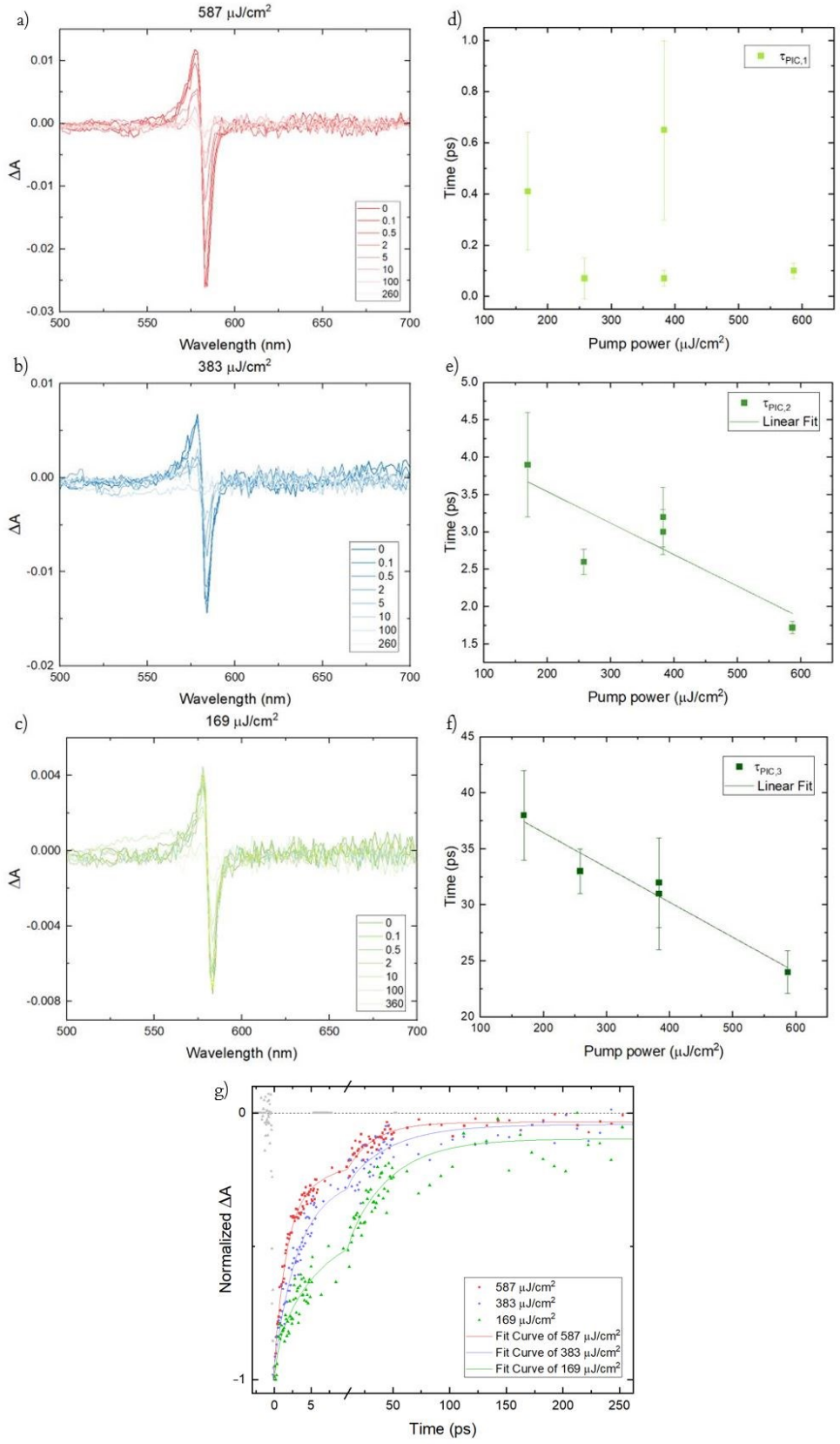

Figure 11.5 In (a), (b), (c) Transient absorption spectra recorded at different delay times (in the legend the delay in ps), using three different pump fluences: 587 μJ/cm² (a), 383 μJ/cm² (b) and 169 μJ/cm²(c). In (d), (e), (f) the time constants retrieved from the three-exponential fitting shown as a function of the pump fluence. The solid line in (e) and (f) represent the fit with equation $y =$

$-0.004 * x + 4.4$ and $y = -0.031 * x + 42.7$ for $\tau_{PIC,2}$ and $\tau_{PIC,3}$, respectively. In (g), the comparison between the GSB decay curves at different pump fluence values. The solid lines represent the decay fittings. Notice the break in the time axis after 10 ps.

A last decay time $\tau_{PIC,4}$, longer than the investigated time window, (>500 ps) is found. We hypothesized it could be caused most likely by residuals of monomeric species and/or possibly fast intersystem crossing to triplet state[63].

11.3 Plexcitons

With the aim to characterize the relaxation processes in different coupling conditions, the dynamics of three different plexciton samples are analyzed with the pump and probe technique. The hybrids are prepared with the same pristine nanorods used as reference. The zero detuning conditions are fulfilled in these samples because the longitudinal plasmon peak falls almost at the same wavelength of the J-aggregates absorption band. Compared to the previous syntheses of hybrids (see Chapter 5 and Section 10.2), in this case the concentration of nanorods is doubled, and the amount of dye molecules as well. This variation was needed in order to reach higher values of absorbance to perform pump and probe measurements. Different quantities of dye molecules are added (see Table 11.2) to a solution of nanorods to achieve different coupling regimes in agreement with the concentration trend previously determined (see Section 10.2.1). According to the previous characterization (Section 10.2.1 and Figure 10.4), the resulting coupling strength will be defined as “very strong”, “strong” and “intermediate” according to the value of the Rabi splitting obtained from the extinction spectra in Figure 11.6.

Table 11.2 Experimental conditions used for the preparation of the nanohybrids with "very strong", "strong" and "intermediate" coupling: volume of dye molecules, wavelength of the plexcitonic peaks and corresponding Rabi splitting Ω_R.

Sample	Dye added (μL)	UP (nm)	LP (nm)	Ω_R (meV)
Very strong	80	543	603	227
Strong	52	550	592	160
Intermediate	28	562	585	87

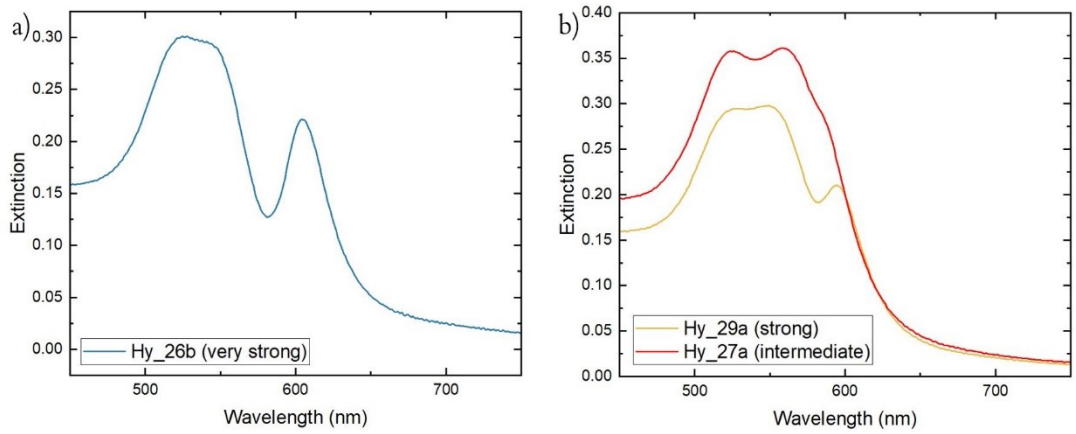

Figure 11.6 Extinction spectra of the three plexcitonic systems analyzed: "very strong" Hy_26b (a, blue line), "strong" Hy_29a (red line) and "intermediate" Hy_27a (yellow line).

11.3.1 Plexcitons in the 'very strong' coupling regime

Transient absorption spectra (Figure 11.7) are collected using three different pump fluences and all are characterized by three negative intense signals, assigned to the GSB of the transversal plasmon peak (at 531 nm), and the two plexcitonic split bands (at 549 and 602 nm) clearly visible also in the extinction spectra of Figure 11.6a.

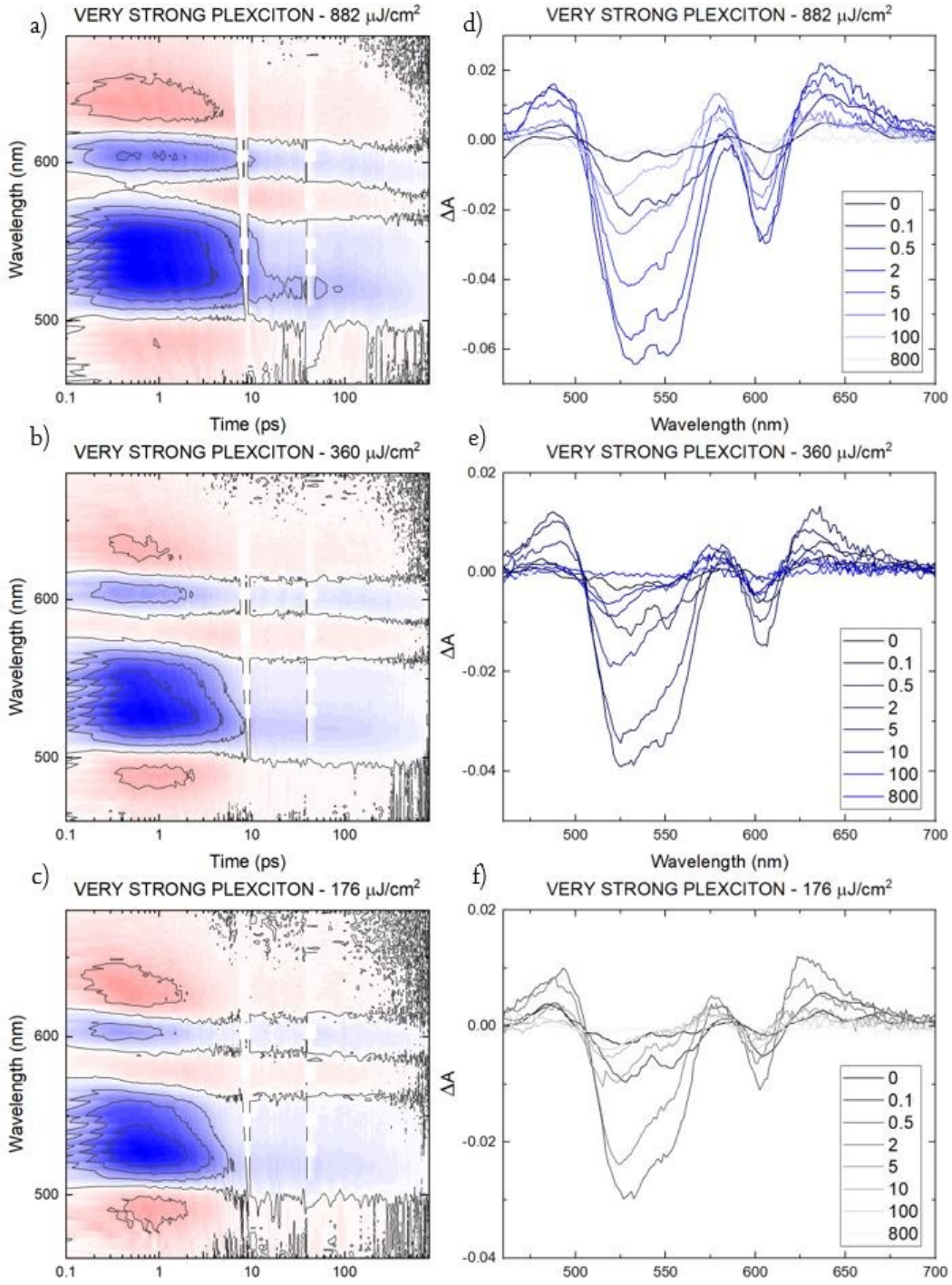

Figure 11.7 Contour plot of the transient spectra of the 'very strong' sample showing the differential absorption (blue-red color scale) as a function of the time and the wavelength (a, b, c) and the transient absorption spectra extracted at different delay times (in the legend the delay in ps) (d, e, f), using three different pump fluences: 882 μJ/cm² (a-d), 360 μJ/cm² (b-e) and 176 μJ/cm²(c-f).

The dynamics of the three GSB signals extracted at wavelengths corresponding to the transverse plasmon (T), UP and LP (Figure 11.8 a,b,c) resemble those of the bare plasmon nanoparticles very closely. Therefore, their time evolution is well fit by the three-time equation used for the nanorods (see Section 8.3) and described by:

i) a fast rise with a time constant $\tau_{verystrong,1}$ (0.232, 0.213 and 0.166 for T, UP and LP, respectively)

ii) a first decay $\tau_{verystrong,2}$ of a few picoseconds (between 2.36 and 6.80 for T, 1.96 and 6.02 for the UP and 1.15-8.01 for the LP).

iii) a third time constant defining the long decay behavior. In this case, no common trend is found for the three peaks. At the three different pump fluences, it seems that the time evolution of the GBSs on the T band and the UP is slowed down compared to the long decay of the plasmonic system alone (see Section 11.1) and does not depend on fluence, with $\tau_{verystrong,3}$(T) = 423 ps and $\tau_{verystrong,3}$(UP) = 644 ps. On the contrary, the decay with time $\tau_{verystrong,3}$(LP) shows a dependence on the pump fluence: the dynamic is very fast for the highest fluences (290 ps is the average of the two measurements). This time is however much slower than in T and UP for medium and low fluences, with a constant decay of 856 ps for the lowest pump fluence.

The time constants obtained from the fitting described above are summarized in Table 11.3 and are shown as a function of the pump fluence in Figure 11.8.

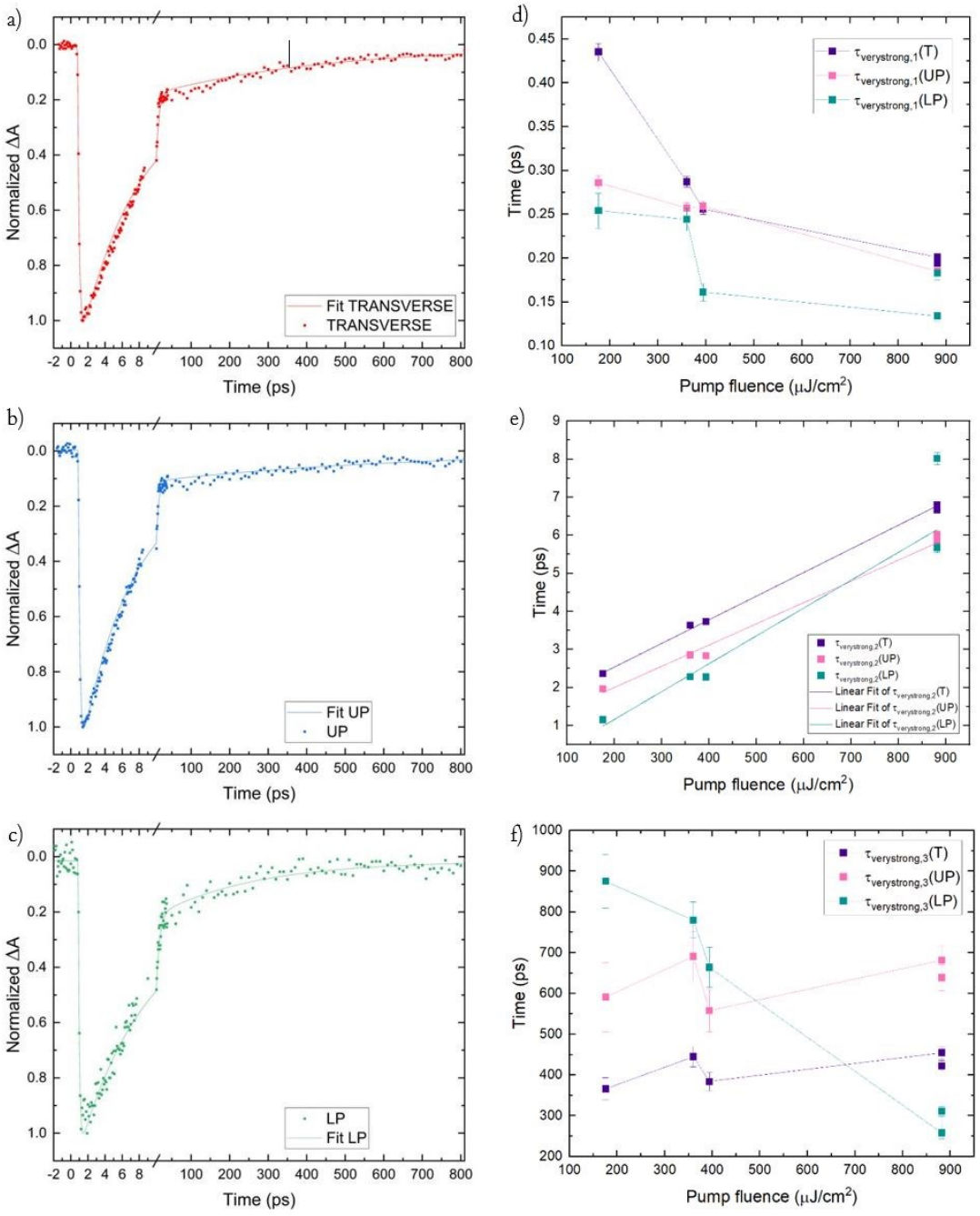

Figure 11.8 In (a, b, c) the comparison between the GSB decay curves extracted at wavelengths corresponding to the T, UP and LP peaks. The solid lines represent the fittings. Notice the break in the time axis at 10 ps. In (d), (e), (f) the time constants retrieved from the three-exponential fitting are shown as a function of the pump fluence. The solid lines in (e) represent the fit with equation $y = 0.0062 * x + 1.30$, $y = 0.0056 * x + 0.9$ *and* $y = 0.007 * x - 0.3$ *for* $\tau_{verystrong,2}$ *of T, UP and LP, respectively.*

Table 11.3 Kinetic constants of the very strong plexcitons for the T, UP and LP peaks. The error on the time constants is estimated to be in the order of 10% from repeated measurements.

VERY STRONG PLEXCITONS			
	Transverse plasmon decay time	Upper polariton decay time	Lower polariton decay time
τ_1	0.232 ps	0.213 ps	0.166 ps
τ_2	2.36 – 6.80 ps	1.96 – 6.02 ps	1.15 – 8.01 ps
τ_3	423 ps	644 ps	856 – 290 ps

As we expected, the two early time constants resemble the nanoparticle $\tau_{nr,1}$ and $\tau_{nr,2}$ (see Section 11.1). Indeed, the excitation wavelength falls at 400 nm where the nanoparticle states prevail and promote the energy transfer to the coupled system. Once again, the dependence on the pump fluence is recognizable on the decay reported with $\tau_{verystrong,2}$ but is less clear for $\tau_{verystrong,1}$. Both of them are ascribed to the processes already explained above (Section 11.1).

On the contrary, it is hypothesized that the slowdown of the dynamics, highlighted by the time constant $\tau_{verystrong,3}$, is due to the exchange of electronic density between plasmon and exciton[55] states and can be explained by the presence of the dark states in the hybrid system. They act as mediators in the energy transfer between the polariton states and hold on to the relaxation processes. This behavior has already been reported in the literature, where the lifetime of the upper and lower bleach signals are commonly reported to be longer for samples with stronger coupling strenght[7,37,55]. Moreover, the lower polariton is sometimes defined as "intrinsically long-lived"[39,40]. Nonetheless, a unified view is not available yet. While further investigations on different nanohybrids are still needed to verify the generality of this phenomenon, our findings suggest that it should be possible to exploit the establishment of the strong coupling regime to control the dynamics of plexciton systems over a significantly large time span. This opens possible

interesting perspectives for effectively using the strong coupling to modify rates of molecular processes and chemically relevant reactions. Indeed, the possibility of slowing down in a controlled way the lifetime of excited states could allow better exploitation of the energy of the excited states to promote relevant photochemical reactions.

After these remarks, the unexpected fast decay of the LP at high fluence is more complicated to explain. A comparison with the literature on excitons coupled with cavities[67–69] suggests that this finding can be ascribed to polariton lasing and Bose-Einstein condensation (BEC), although no evidence has yet been reported for excitons coupled with plasmon nanoparticles. Interestingly, the hypothesis can be upheld by the evidence of blue-shift of the LP peak in time (see Figure 11.9), which is related to the reduction of the coupling strength caused by the BEC process[68].

However, this attribution should be investigated with further experiments and especially confirmed by fluorescence measurements.

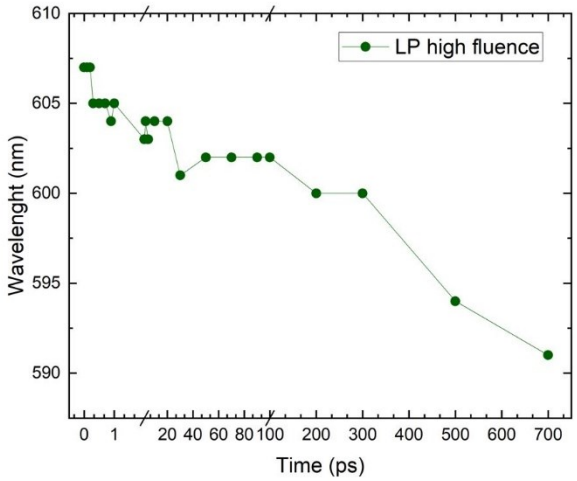

Figure 11.9 Peak wavelength of the LP in the very strong sample at high fluence (882 μJ/cm²) as a function of the delay time. A blue shift to shorter wavelengths is clearly recognizable.

A final remark is that UP and LP must be supposed to be related as they are populated at the same time and decay in a similar way, in the investigated time

window. This result supports the hypothesis of the presence of a coherent energy exchange between excitons and plasmons[37,55]. Also in this case, additional measurements capable of directly quantifying the coherent dynamics must be performed to confirm this hypothesis. Nonetheless, these preliminary pump-probe data are extremely promising in view of possible quantum-nano-photonic applications that require the preparation, control, and tuning of the coherent behavior of complex systems.

11.3.2 Strong and intermediate coupled plexcitons

Even strong and intermediate samples mentioned above are analyzed with transient absorption spectroscopy by using three different values of pump fluence. The contour plots of the transient absorption spectra and the differential absorption spectra at different delay times are shown in Figure 11.10. It can be noticed that the transient signal is particularly weak for the measurements at low pump fluence, so in the following we will focus our attention on the results obtained at high pump fluence.

In this case, the kinetic decay of the GSBs at the T (529 nm) and the UP wavelengths (552 nm and 565 nm for the strong and the intermediate, respectively) is analyzed with the three-times decay equation used for the nanorods (see Chapter 8.3). Again, the resulting time constants, shown in Table 11.4, reflect the nanoparticle dynamics for the first 10 ps, while the third decay constant assumes values faster than the very strong coupled plexciton and slower than the plasmonic system. The result is consistent with previous outcomes and can be easily justified considering that in this case the states are coupled more weakly than in the very strongly coupled system described before. The fluence dependence of τ_2 is recognizable as in the previous cases ($\tau_{nr,2}$ and $\tau_{verystrong,\,2}$).

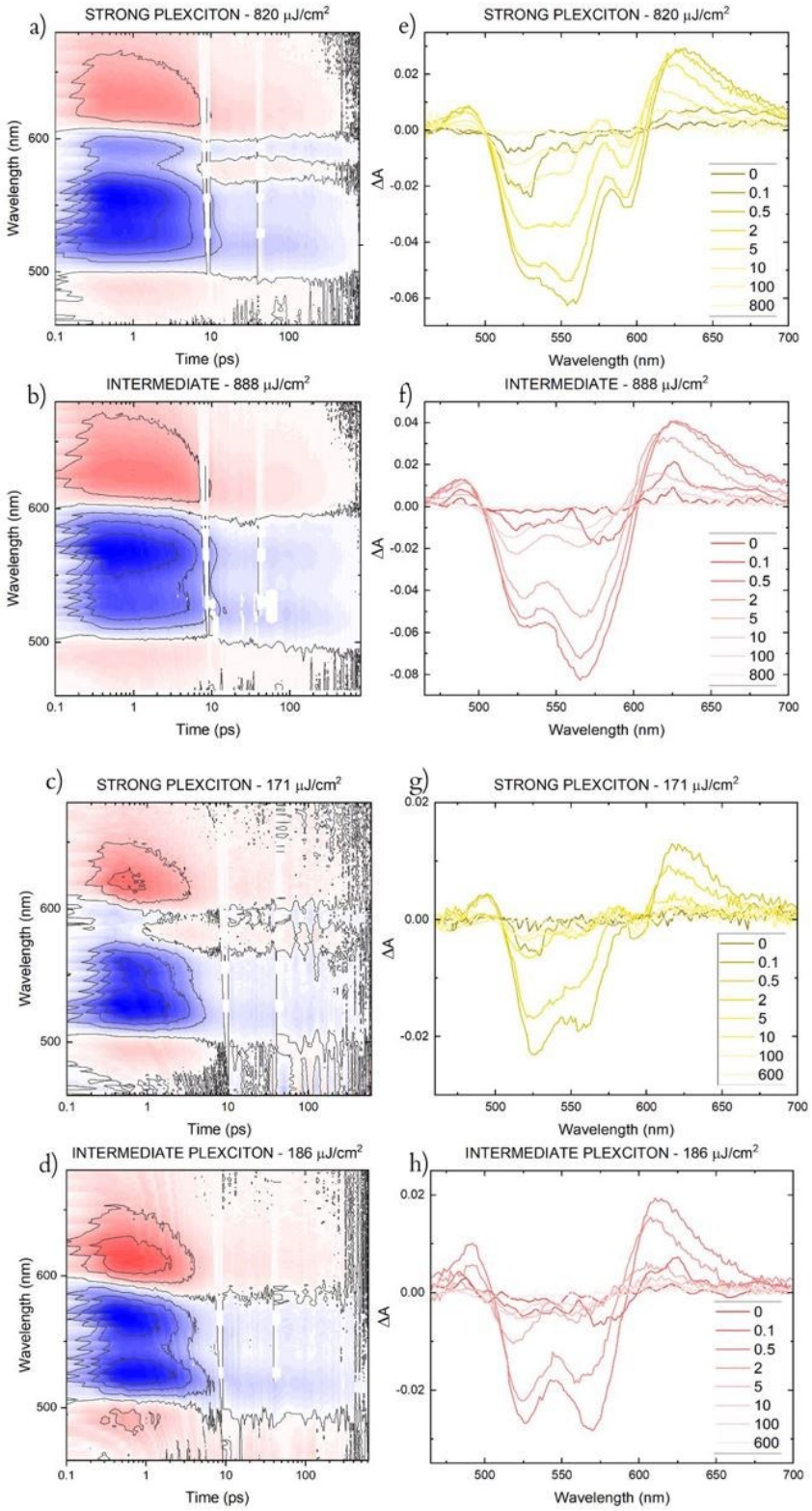

Figure 11.10 Contour plots of the transient spectra of the 'strong' (yellow) and 'intermediate' (red) samples showing the differential absorption (blue-red color scale) as a function of the time and the wavelength (a, b, c, d). Transient absorption spectra recorded at different delay times (in the legend the delay in ps) (e, f, g, h), using different pump fluences: 820 μJ/cm² (a, e), 888 μJ/cm² (b-f), 171 μJ/cm² (c-g) and 186 μJ/cm²(d-h).

Table 11.4 Kinetic constants obtained for the strong and the intermediate plexcitons samples for the T, UP and LP peaks. The error on the time constants is estimated to be in the order of 10% from repeated measurements.

STRONG AND INTERMEDIATE PLEXCITONS at high fluence						
	Transversal decay time (ps)		Upper polariton decay time (ps)		Lower polariton decay time (ps)	
	STRONG	INTERMEDIATE	STRONG	INTERMEDIATE	STRONG	INTERMEDIATE
τ_1	0.197	0.165	-	0.165	0.186	-
τ_2	6.2	7.93	5.33	6.74	4.8	-
τ_3	371	328	463	464	427 $\tau_{additional}$ = 46 ps	-

Interestingly, a new feature appears in the decay dynamics of the LP GBS signals, which falls at 593 nm and 589 nm for the strong and intermediate samples, respectively (Figure 11.11).

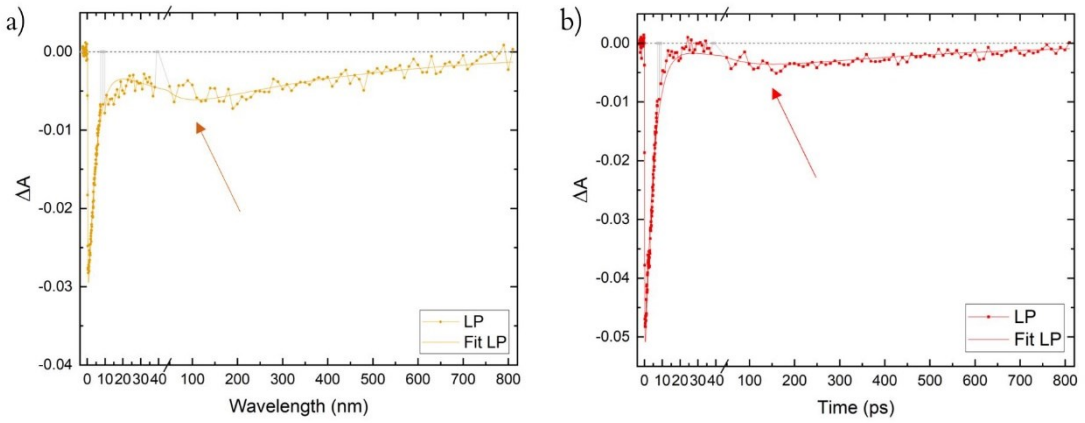

Figure 11.11 Comparison between the GSB decay curve of the LP peaks in the strong (a, yellow) and intermediate (b, orange) samples. The solid lines represent the decay fittings. The arrows indicate the additional rise time.

The presence of an additional rise time (highlighted by the arrows in Figure 11.11) requires the use of Equation 11.1 for the fitting, from which the time constants in Table 11.4 are extracted.

$$\Delta A = \Delta A_0 + A_0 * \left(1 - e^{-\frac{t-t_0}{\tau_{i,1}}}\right) * e^{-\frac{t}{\tau_{i,2}}} + A_2 * e^{-\frac{t}{\tau_{i,3}}} + A_3 * e^{-\frac{t}{\tau_{additional}}} \qquad \text{Eq. 11.1}$$

While in the early 10 ps the dynamics show no significant differences with respect to pristine nanorods and previous samples, it is worth noting that in this case the LP seems to get populated later than the UP. An explanation of this dynamic process has yet to be found since the simple hypothesis that the state is populated directly from the UP is not upheld by analyses of the UP dynamics, which doesn't show a corresponding decay time. Still, the discovery of this additional kinetic component marks the fact that the coupling strength is reduced in these samples and the system can no longer exchange energy coherently.

11.4 Final remarks on pump-probe measurements

The transient absorption spectroscopy measurements carried out on plexcitonic samples prepared in different coupling regimes allowed for a comprehensive spectroscopic characterization of this fascinating family of nanohybrids. It was found that the system exhibits significantly different behaviors in the different coupling conditions and measurements at different pump fluences highlighted that these features change according to the excitation energy provided. Although a more in-depth analysis of the captured phenomena is required, the relaxation dynamics have in general been depicted, succeeding in highlighting any dependencies on fluence.

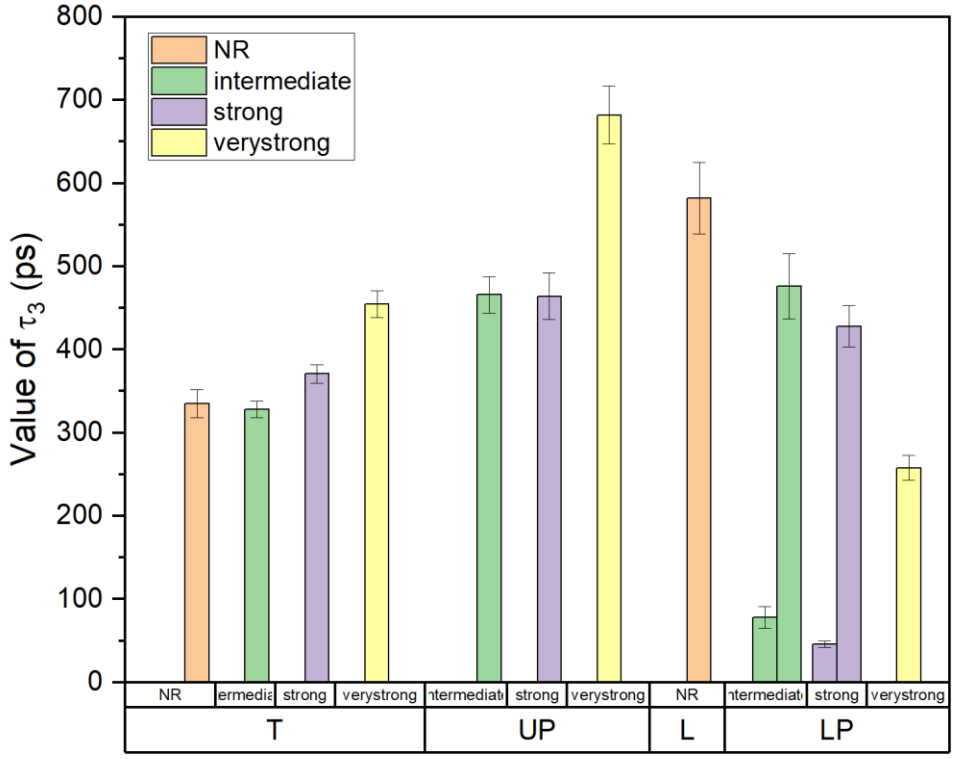

Figure 11.12 Histogram summarizing the time constants found for the long decay of the plexcitons at high fluence (882, 820 and 880 μJ/cm² for the very strong (yellow), the strong (violet) and the intermediate (green) samples). While the T long decay is similar to the nanorods (orange), the UP and LP have different values with respect to the longitudinal time decay (L) of the pristine nanorods. In particular, it is worth noting that the value of UP and LP decay time is very similar between the strong and the intermediate plexciton. On the contrary, for the very strong sample a significant difference between the UP and LP emerges. A possible explanation refers to the proximity of the energy levels: for the intermediate and the strong coupling, the energy levels are closer and the resulting relaxation time is quite similar; on the contrary, in the very strong coupled sample the largest splitting of the levels causes a very different time constant of relaxation.

An overview of the main dynamical constants found for the plexcitonic nanohybrids in different coupling regimes compared with their non-interacting constituents is provided in Figure 11.12. At a first look it is immediately clear that in the 'very strong' coupled systems UP and LP present significantly different time trends, confirming the possibility of really engineering the dynamic behavior by tuning in a controlled way the coupling regime.

The chosen plexcitonic nanomaterials have proved to be a controllable and adaptable family of nanosystems to the most varied experimental needs. The results

obtained are particularly interesting, dealing with a topic that has not yet been deeply investigated in the literature, but which already demonstrates enormous potential.

Conclusions and future perspectives

This Thesis has succeeded in fulfilling its initial objectives.

First of all, a successful protocol has been developed and optimized for the synthesis of gold nanorods, including an oxidation step to obtain nanoparticles with wanted properties in a predictable and controlled way. A lot of attention has been paid to comprehending the molecular mechanisms at the base of the synthetic procedures to gain enough knowledge to control the reaction mechanism and predict the results. Although an exhaustive explanation of the specific trends recorded during the oxidation procedure could not be found because of the complexity of the mechanisms involved, it was anyway possible to suggest a specific method to ensure the achievement of oxidized nanorods with wanted properties. This procedure will be highly beneficial also in future work because it will allow us to foresee with reasonable predictability the experimental conditions to follow to prepare nanorods characterized by longitudinal plasmon resonances at specific wavelengths. This issue is particularly crucial in preparing strongly coupled plexcitonic nanohybrids because one of the main prerequisites to reaching the strong coupling regime is to achieve the resonance between the plasmon and the exciton wavelengths. The exciton wavelength is not easily tuneable because only a limited choice of molecular dyes is so far available. Therefore, being able to prepare nanoparticles with a plasmon resonance easily tuneable to match the wavelength of the molecular exciton is highly valuable and will favor the preparation of a vast library of plexciton nanohybrids necessary for a systematic investigation of the photophysical and dynamic properties of these still underexplored but highly promising nanomaterials.

Second, the right combinations of nanorods and molecular dyes and the supramolecular conditions necessary to promote the effective establishment of the strong coupling regime have been optimized.

Indeed, an easy procedure to control the coupling strength has been found. It was thus possible to prepare nanohybrids characterized by different coupling strengths. In the Thesis we focused in particular on three samples whose coupling is defined as 'very strong', 'strong' and 'intermediate' in accordance with the current definitions accepted in the literature.

The photophysical and dynamic behaviour of these three samples has been thoroughly investigated by linear and time-resolved non-linear (pump and probe) techniques. The transient signals and the photoinduced relaxation dynamics have been characterized as a function of the coupling regime and analyzed at different pump fluences, in the quest for specific dependencies of the dynamic behaviour on experimental conditions and coupling regimes. We found that the 'very strong' coupling system exhibits a significantly different dynamic and fluence-dependent behavior than the other two samples, while the 'strong' and the 'intermediate' samples seem instead to behave in a similar way.

On the one hand, these findings provide a first important conclusion: it is really possible to engineer the dynamic behavior of nanohybrids samples by tuning in a controlled way their coupling regime. This opens possible interesting perspectives for effectively using the strong coupling to modify rates of molecular processes and chemically relevant reactions, which is one of the most promising envisioned applications of plexcitonic nanosystems.

On the other hand, these collected pieces of evidence raise a more subtle question about the definition of the coupling regimes. In Chapter 1 we discussed the conventionally accepted definitions of strong coupling regime based on the 'static' value of quantum mechanical parameters such as dissipation rates and coupling strength. In the literature, we are already assisting in a strong debate about the correctness of these definitions and a plethora of alternative definitions has been proposed by the different authors for different systems. Our data suggest that a more practical and helpful definition should at least account for 'dynamic'

parameters, such as the ultrafast behavior recorded in pump-probe experiments and the manifested dependence on pump fluence. This will allow for a clearer and less ambiguous classification of several sub-families of strongly coupled systems. Future additional investigations on different analogous nanosystems will be necessary to support this important claim.

References

1. Manuel, A. P., Kirkey, A., Mahdi, N. & Shankar, K. Plexcitonics-fundamental principles and optoelectronic applications. *J. Mater. Chem. C* **7**, 1821–1853 (2019).

2. Das, K., Dey, J., Verma, M. S., Kumar, M. & Chandra, M. Probing the role of oscillator strength and charge of exciton forming molecular J-aggregates in controlling nanoscale plasmon-exciton interactions. *Phys. Chem. Chem. Phys.* **22**, 20499–20506 (2020).

3. Tokmakoff, A. Time-Dependent Quantum Mechanics and Spectroscopy. *Lecture* 272 (2014).

4. Marquier, F., Sauvan, C. & Greffet, J. J. Revisiting quantum optics with surface plasmons and plasmonic resonators. *ACS Photonics* **4**, 2091–2101 (2017).

5. Amendola, V., Pilot, R., Frasconi, M., Maragò, O. M. & Iatì, M. A. Surface plasmon resonance in gold nanoparticles: A review. *J. Phys. Condens. Matter* **29**, (2017).

6. Boriskina, S. V. *et al.* Losses in plasmonics: from mitigating energy dissipation to embracing loss-enabled functionalities. *Adv. Opt. Photonics* **9**, 775 (2017).

7. Ribeiro, R. F., Martínez-Martínez, L. A., Du, M., Campos-Gonzalez-Angulo, J. & Yuen-Zhou, J. Polariton chemistry: controlling molecular dynamics with optical cavities. *Chem. Sci.* **9**, 6325–6339 (2018).

8. Pérez-Juste, J., Pastoriza-Santos, I., Liz-Marzán, L. M. & Mulvaney, P. Gold nanorods: Synthesis, characterization and applications. *Coord. Chem. Rev.* **249**, 1870–1901 (2005).

9. Peruffo, N. Colloidal Plexcitonic Materials: Design and dynamics. 1–120 (2021).

10. Kobayashi, T. *J-Aggregates*. (WORLD SCIENTIFIC, 1996). doi:10.1142/3168.

11. Bricks, J. L., Slominskii, Y. L., Panas, I. D. & Demchenko, A. P. Fluorescent J-aggregates of cyanine dyes: Basic research and applications review. *Methods Appl. Fluoresc.* **6**, (2018).

12. Moll, J., Daehne, S., Durrant, J. R. & Wiersma, D. A. Optical dynamics of excitons in J aggregates of a carbocyanine dye. *J. Chem. Phys.* **102**, 6362–6370 (1995).

13. Törmä, P. & Barnes, W. L. Strong coupling between surface plasmon polaritons and emitters: A review. *Reports Prog. Phys.* **78**, (2015).

14. Liu, R. *et al.* Strong Light-Matter Interactions in Single Open Plasmonic Nanocavities at the Quantum Optics Limit. *Phys. Rev. Lett.* **118**, 1–6 (2017).

15. Vasa, P. *et al.* Real-time observation of ultrafast Rabi oscillations between excitons and plasmons in metal nanostructures with J-aggregates. *Nat. Photonics* **7**, 128–132 (2013).

16. Kolaric, B., Maes, B., Clays, K., Durt, T. & Caudano, Y. Strong Light–Matter Coupling as a New Tool for Molecular and Material Engineering: Quantum Approach. *Adv. Quantum Technol.* **1**, 1800001 (2018).

17. Baranov, D. G., Wersäll, M., Cuadra, J., Antosiewicz, T. J. & Shegai, T. Novel Nanostructures and Materials for Strong Light-Matter Interactions. *ACS Photonics* **5**, 24–42 (2018).

18. Xu, D. *et al.* Quantum plasmonics : new opportunity in fundamental and applied photonics. *Adv. Opt. photonics* **10**, 703–756 (2019).

19. Hertzog, M., Wang, M., Mony, J. & Börjesson, K. Strong light-matter interactions: A new direction within chemistry. *Chem. Soc. Rev.* **48**, 937–961 (2019).

20. Tame, M. S. *et al.* Quantum plasmonics. *Nat. Phys.* **9**, 329–340 (2013).

21. Salomon, A., Genet, C. & Ebbesen, T. W. Molecule-light complex: Dynamics of hybrid molecule-surface plasmon states. *Angew. Chemie - Int. Ed.* **48**, 8748–8751 (2009).

22. Wiederrecht, G. P., Hall, J. E. & Bouhelier, A. Control of molecular energy redistribution pathways via surface plasmon gating. *Phys. Rev. Lett.* **98**, 1–4

(2007).

23. Gómez, D. E., Lo, S. S., Davis, T. J. & Hartland, G. V. Picosecond kinetics of strongly coupled excitons and surface plasmon polaritons. *J. Phys. Chem. B* **117**, 4340–4346 (2013).

24. Fofang, N. T., Grady, N. K., Fan, Z., Govorov, A. O. & Halas, N. J. Plexciton Dynamics: Exciton–Plasmon Coupling in a J-Aggregate–Au Nanoshell Complex Provides a Mechanism for Nonlinearity. *Nano Lett.* **11**, 1556–1560 (2011).

25. Balci, S. *et al.* Tunable Plexcitonic Nanoparticles: A Model System for Studying Plasmon-Exciton Interaction from the Weak to the Ultrastrong Coupling Regime. *ACS Photonics* **3**, 2010–2016 (2016).

26. Manuel, A., Kirkey, A., Mahdi, N. & Shankar, K. Plexcitonics – Fundamental principles and optoelectronic applications. *J. Mater. Chem. C* (2018) doi:2018/TC/C8TC05054F.

27. Grynberg, G., Aspect, A., Fabre, C. & cohen-tannoudji, C. Introduction to Quantum Optics: From the Semi-classical Approach to Quantized Light. in (2010).

28. Melnikau, D. *et al.* Rabi Splitting in Photoluminescence Spectra of Hybrid Systems of Gold Nanorods and J-Aggregates. *J. Phys. Chem. Lett.* **7**, 354–362 (2016).

29. Yoshida, A., Uchida, N. & Kometani, N. Synthesis and spectroscopic studies of composite gold nanorods with a double-shell structure composed of spacer and cyanine dye J-aggregate layers. *Langmuir* **25**, 11802–11807 (2009).

30. Kumar, M., Dey, J., Verma, M. S. & Chandra, M. Nanoscale plasmon-exciton interaction: The role of radiation damping and mode-volume in determining coupling strength. *Nanoscale* **12**, 11612–11618 (2020).

31. Zengin, G. *et al.* Approaching the strong coupling limit in single plasmonic nanorods interacting with J-aggregates. *Sci. Rep.* **3**, 1–8 (2013).

32. Liu, R. *et al.* Strong Light-Matter Interactions in Single Open Plasmonic Nanocavities at the Quantum Optics Limit. *Phys. Rev. Lett.* **118**, 1–41 (2017).

33. Stete, F. Gold at the nanoscale. (2020). doi:10.25932/publishup-49605.

34. Peruffo, N., Parolin, G., Collini, E., Corni, S. & Mancin, F. Engineering the aggregation of dyes on ligand-shell protected gold nanoparticles to promote plexcitons formation. *Nanomaterials* **12**, 1180 (2022).

35. Peruffo, N., Mancin, F. & Collini, E. Plexcitonic Nanohybrids Based on Gold Nanourchins: the Role of the Capping Layer. *J Phys Chem C* **125**, 19897–19905 (2021).

36. Peruffo, N., Gil, G., Corni, S., Mancin, F. & Collini, E. Selective switching

of multiple plexcitons in colloidal materials: Directing the energy flow at the nanoscale. *Nanoscale* **13**, 6005–6015 (2021).

37. Balci, S. *et al.* Probing ultrafast energy transfer between excitons and plasmons in the ultrastrong coupling regime. *Appl. Phys. Lett.* **105**, (2014).

38. Simon, T. *et al.* Exploring the Optical Nonlinearities of Plasmon-Exciton Hybrid Resonances in Coupled Colloidal Nanostructures. *J. Phys. Chem. C* **120**, 12226–12233 (2016).

39. Schwartz, T. *et al.* Polariton dynamics under strong light-molecule coupling. *ChemPhysChem* **14**, 125–131 (2013).

40. Canaguier-Durand, A., Genet, C., Lambrecht, A., Ebbesen, T. W. & Reynaud, S. Non-Markovian polariton dynamics in organic strong coupling. *Eur. Phys. J. D* **69**, 1–6 (2015).

41. Virgili, T. *et al.* Ultrafast polariton relaxation dynamics in an organic semiconductor microcavity. *Phys. Rev. B - Condens. Matter Mater. Phys.* **83**, 2–7 (2011).

42. Beeby, A. Pump-Probe Laser Spectroscopy. in *An Introduction to Laser Spectroscopy: Second Edition* (eds. Andrews, D. L. & Demidov, A. A.) 105–137 (Springer US, 2002). doi:10.1007/978-1-4615-0727-7_4.

43. Collini, E. 2D Electronic Spectroscopic Techniques for Quantum Technology Applications. *J. Phys. Chem. C* **125**, 13096–13108 (2021).

44. Bolzonello, L. Ultrafast relaxation dynamics of multichromophoric systems through advanced optical spectroscopies. (2016).

45. Del Fatti, N. *et al.* Nonequilibrium electron dynamics in noble metals. *Phys. Rev. B - Condens. Matter Mater. Phys.* **61**, 16956–16966 (2000).

46. Scarabelli, L., Sánchez-Iglesias, A., Pérez-Juste, J. & Liz-Marzán, L. M. A 'Tips and Tricks' Practical Guide to the Synthesis of Gold Nanorods. *J. Phys. Chem. Lett.* **6**, 4270–4279 (2015).

47. Nikoobakht, B. & El-Sayed, M. A. Preparation and growth mechanism of gold nanorods (NRs) using seed-mediated growth method. *Chem. Mater.* **15**, 1957–1962 (2003).

48. Liu, M. & Guyot-Sionnest, P. Mechanism of silver(I)-assisted growth of gold nanorods and bipyramids. *J. Phys. Chem. B* **109**, 22192–22200 (2005).

49. Jana, N. R., Gearheart, L. & Murphy, C. J. Seed-mediated growth approach for shape-controlled synthesis of spheroidal and rod-like gold nanoparticles using a surfactant template. *Adv. Mater.* **13**, 1389–1393 (2001).

50. Lohse, S. E. & Murphy, C. J. The quest for shape control: A history of gold nanorod synthesis. *Chem. Mater.* **25**, 1250–1261 (2013).

51. Almora-Barrios, N., Novell-Leruth, G., Whiting, P., Liz-Marzán, L. M. & López, N. Theoretical description of the role of halides, silver, and surfactants on the structure of gold nanorods. *Nano Lett.* **14**, 871–875 (2014).

52. Rodríguez-Fernández, J., Pérez-Juste, J., Mulvaney, P. & Liz-Marzán, L. M. Spatially-directed oxidation of gold nanoparticles by Au(III)-CTAB complexes. *J. Phys. Chem. B* **109**, 14257–14261 (2005).

53. Ward, C. J., Tronndorf, R., Eustes, A. S., Auad, M. L. & Davis, E. W. Seed-mediated growth of gold nanorods: Limits of length to diameter ratio control. *J. Nanomater.* **2014**, (2014).

54. Melnikau, D. *et al.* Double Rabi Splitting in a Strongly Coupled System of Core-Shell Au@Ag Nanorods and J-Aggregates of Multiple Fluorophores. *J. Phys. Chem. Lett.* **10**, 6137–6143 (2019).

55. Balci, S. *et al.* Tunable Plexcitonic Nanoparticles: A Model System for Studying Plasmon-Exciton Interaction from the Weak to the Ultrastrong Coupling Regime. *ACS Photonics* **3**, 2010–2016 (2016).

56. Hartland, G. V. Optical studies of dynamics in noble metal nanostructures. *Chem. Rev.* **111**, 3858–3887 (2011).

57. Finkelstein-Shapiro, D. *et al.* Understanding radiative transitions and relaxation pathways in plexcitons. *Chem* **7**, 1092–1107 (2021).

58. Link, S., Burda, C., Mohamed, M., Nikoobakht, B. & El-Sayed, M. Femtosecond transient-absorption dynamics of colloidal gold nanorods: Shape independence of the electron-phonon relaxation time. *Phys. Rev. B - Condens. Matter Mater. Phys.* **61**, 6086–6090 (2000).

59. Link, S. & El-Sayed, M. A. Shape and size dependence of radiative, non-radiative and photothermal properties of gold nanocrystals. *Int. Rev. Phys. Chem.* **19**, 409–453 (2000).

60. Hodak, J., Martini, I. & Hartland, G. V. Ultrafast study of electron-phonon coupling in colloidal gold particles. *Chem. Phys. Lett.* **284**, 135–141 (1998).

61. Yağlioğlu, G., Dorsinville, R. & Özçelik, S. Femtosecond response of J aggregates adsorbed onto silver colloid surfaces. *J. Appl. Phys.* **94**, 3143–3146 (2003).

62. Virgili, T. *et al.* Role of intramolecular dynamics on intermolecular coupling in cyanine dye. *Phys. Rev. B - Condens. Matter Mater. Phys.* **81**, 1–6 (2010).

63. Kopainsky, B. & Kaiser, W. Ultrafast transient processes of monomers, dimers, and aggregates of pseudoisocyanine chloride (PIC). *Chem. Phys. Lett.* **88**, 357–361 (1982).

64. Kobayashi, S. & Sasaki, F. Dynamical properties of large coherence length excitons in picj aggregates. *Jpn. J. Appl. Phys.* **34**, 279–281 (1995).

65. Fidder, H., Knoester, J. & Wiersma, D. A. Observation of the one-exciton to two-exciton transition in a J aggregate. *J. Chem. Phys.* **98**, 6564–6566 (1993).

66. Homgtet, M. & Quitevis, E. L. Excited-State Dynamics of Polymer-Bound J-Aggregates. 12408–12415 (1993).

67. Deveaud-Plédran, B. On the condensation of polaritons. *J. Opt. Soc. Am. B* **29**, A138 (2012).

68. Kasprzak, J. *et al.* Bose-Einstein condensation of exciton polaritons. *Nature* **443**, 409–414 (2006).

69. Kéna-Cohen, S. & Forrest, S. R. Room-temperature polariton lasing in an organic single-crystal microcavity. *Nat. Photonics* **4**, 371–375 (2010).